

# ANNA: a toolbox for Newtonian Noise Analysis

P. Reumers<sup>a,1</sup>, X. Kuci<sup>a,1,\*</sup>, S. François<sup>a</sup>, G. Degrande<sup>a</sup>

<sup>a</sup>*KU Leuven, Department of Civil Engineering, Structural Mechanics Section, Kasteelpark Arenberg 40, Leuven, B-3001, Belgium*

---

## Abstract

The Einstein Telescope (ET) is a third-generation underground gravitational wave observatory designed to achieve an unprecedented sensitivity down to 3 Hz. Waves propagating in the soil due to anthropogenic or natural vibration sources generate density fluctuations which cause gravitational attraction, resulting in motion of the mirrors of the laser interferometer known as Newtonian noise. The latter is computed by integrating density fluctuations due to seismic wave fields over the soil domain surrounding the test mass.

**ANNA Newtonian Noise Analysis** is a toolbox that computes Newtonian Noise from a seismic wave field defined on a finite element mesh, using Gaussian quadrature. 3D finite element meshes composed of linear and quadratic tetrahedral (4-node and 10-node) and brick (8-node and 20-node) elements are supported. The user computes (or interpolates) a seismic wave field on a finite element mesh and the toolbox computes the total Newtonian noise, as well as the bulk and surface contributions. ANNA runs in the MATLAB programming and numeric computing platform and is compatible with the open-source GNU Octave Scientific Programming Language; a Python version is also available.

The toolbox is verified for plane P- and S-waves propagating in an elastic homogeneous full space with a mirror suspended in a spherical cavity, assuming that the wavelength is much larger than the radius of the cavity, so that wave scattering can be ignored. Excellent agreement with analytical solutions is obtained. Similar good agreement is reported for the Newtonian noise on a test mass suspended at a finite distance above the free surface of a homogeneous elastic halfspace in which a Rayleigh wave propagates.

The proposed finite element framework provides a physically consistent and computationally efficient approach for computing gravitational-seismic coupling in heterogeneous media.

*Keywords:* Einstein Telescope, Newtonian noise, seismic wave propagation, finite element formulation

---



---

\*Corresponding author

*Email addresses:* [pieter.reumers@kuleuven.be](mailto:pieter.reumers@kuleuven.be) (P. Reumers), [georgia.kuci@kuleuven.be](mailto:georgia.kuci@kuleuven.be) (X. Kuci), [stijn.francois@kuleuven.be](mailto:stijn.francois@kuleuven.be) (S. François), [geert.degrande@kuleuven.be](mailto:geert.degrande@kuleuven.be) (G. Degrande)

<sup>1</sup>These authors should be regarded as joint first authors.

## 1. Introduction

The Einstein Telescope is a third-generation gravitational wave detector that is planned to be constructed in the coming decade [1]. It consists of an underground triangular laser interferometer and is designed to observe gravitational waves – ripples in the 4D space-time continuum – due to e.g. binary black hole or binary neutron star mergers. The mirrors of the laser interferometer are installed in suspension towers placed inside large caverns at the corner points of the interferometer.

To observe gravitational waves caused by mergers at a larger distance or with a larger mass, the sensitivity and operating frequency range (above 10 Hz) of second-generation gravitational wave detectors such as LIGO and Virgo are insufficient [1]. In order to improve the sensitivity by one order of magnitude and to reduce the operating frequency to 3 Hz, the Einstein Telescope is preferably constructed underground in a seismically quiet region [2] so that disturbance by anthropogenic vibration sources such as road and railway traffic, wind turbines, quarries, industry and construction activities is maximally reduced.

Seismic Newtonian noise dominates at low frequencies: seismic waves propagating in the soil generate density fluctuations, which result in gravitational attraction and corresponding motion of the mirrors of the laser interferometer. Since these gravitational forces cannot be shielded, the only mitigation measure is to estimate Newtonian noise from seismic measurements through wave field reconstruction and to subtract it from the interferometer data [3].

Analytical solutions for Newtonian noise are available for simplified problems involving plane harmonic P- or S-waves propagating in a homogeneous linear elastic full space [4], assuming that the wavelength is much larger than the dimensions of the cavity so that wave scattering can be neglected. Harms [4] also derived an analytical solution for the Newtonian noise on a mirror suspended at a finite distance above the free surface of a homogeneous linear elastic halfspace, excited by a harmonic Rayleigh wave. In practice, however, the topology and geology of a site are more complicated, involving hills, valleys, stratification due to sedimentation processes, as well as folding of soil and rock layers. Seismic wave fields are caused by a variety of anthropogenic vibration sources and affected by the soil's topology and layering, as well as the interferometer's caverns, tunnels, and shafts. As a result, numerical methods are required to compute the seismic wave field and the corresponding Newtonian Noise.

Several methods are available to compute a three-dimensional (3D) seismic wave field due to anthropogenic vibration sources, accounting for dynamic soil-structure interaction. A direct stiffness formulation or thin layer method [5], as implemented in the ElastoDynamics Toolbox for MATLAB [6], is used to model surface waves or forced vibration due to harmonic or transient excitation in horizontally layered media. Vibration due to road and railway traffic can be computed with the TRAFFIC toolbox in MATLAB, which couples a semi-analytical road or track model to a two-and-a-half (2.5D) dimensional boundary element (BE) model of the layered soil [7, 8, 9]; alternatively the MOTIV [10, 11, 12] and MEFISSTO [13] packages can be used. 3D finite element formulations equipped with infinite elements, absorbing boundary conditions or perfectly matched layers [14, 15, 16, 17], cou-

pled finite element-boundary element formulations [18, 13, 19] and spectral element models such as SPECFEM3D and SPEED [20] can be employed to solve more complicated dynamic soil-structure interaction problems, such as vibration caused by trains running on bridges or by wind turbines and wave scattering by the interferometer’s caverns, tunnels and shafts.

Assuming that the seismic wave field is computed or interpolated on a 3D finite element mesh, this paper presents the **ANNA Newtonian Noise Analysis** toolbox that predicts the Newtonian noise on a mirror by means of a 3D finite element formulation. The volume integral that quantifies the total Newtonian noise of the seismic wave field is computed by means of Gaussian quadrature, together with the bulk and surface contributions. This finite element formulation is verified by means of the aforementioned analytical formulations. We consider the Newtonian noise on a mirror suspended in a spherical cavity in a homogeneous linear elastic full space, excited by plane P- or S-waves [4], as well as a mirror suspended at a finite distance above the free surface of a homogeneous linear elastic halfspace, excited by a Rayleigh wave [4].

The paper is organized as follows. Section 2 presents expressions for the total derivative of the gravitational potential, as well as total Newtonian noise which is decomposed in a bulk and surface contribution. Section 3 develops a finite element formulation to evaluate the Newtonian noise for a seismic wave field defined on a finite element mesh. Expressions are derived for finite element matrices that, when multiplied with the seismic displacement vector, result in the total Newtonian noise, as well as the bulk and surface contribution. Section 4 presents the verification of the proposed finite element formulation by means of problems for which an analytical solution is available. Particular attention is paid to adequate finite element mesh refinement in order to guarantee accurate evaluation of the Newtonian noise. Section 5 summarizes the conclusions of the paper.

## 2. Theoretical background

Seismic Newtonian noise is the undesired motion (acceleration) caused by gravitational attraction of the mirror of the laser interferometer due to density fluctuations in the soil, that are caused by seismic wave fields.

### 2.1. Gravitational potential

The gravitational force  $F$  between two point masses  $M$  and  $m$  at a distance  $r$  is equal to:

$$F = G \frac{Mm}{r^2} \quad (1)$$

where  $G \approx 6.6743 \times 10^{-11} \text{ m}^3/\text{kg}/\text{s}^2$  is the gravitational constant. The gravitational potential  $\phi(r)$  [Nm/kg] is defined as the work per unit mass  $m$  required to move this mass  $m$  from infinity (where  $\phi = 0$ ) to a distance  $r$  from the mass  $M$ :

$$\phi(r) = \frac{1}{m} \int_{+\infty}^r G \frac{Mm}{x^2} dx = -G \frac{M}{r} \quad (2)$$

The value of  $\phi(r)$  is negative as work is required to pull objects away from large masses.

In equation (2), the mass  $m$  can be interpreted as the mass of a mirror of the laser interferometer at position  $\mathbf{x}_0$ . Furthermore, the point mass  $M$  is replaced by a set of particles that at time  $t = 0$  are contained in a volume  $\Omega(\mathbf{X})$ , where  $\mathbf{X}$  are the coordinates in the reference configuration. When a dynamic excitation causes a seismic wave field, this set of particles moves and, at time  $t$ , is contained in a volume  $\Omega(\mathbf{x}, t)$  in the actual configuration  $\mathbf{x}$ . The gravitational potential  $\phi(\mathbf{x}_0, t)$  at the position  $\mathbf{x}_0$  of the mirror with mass  $m$ , or the work per unit mass  $m$ , is then expressed as:

$$\phi(\mathbf{x}_0, t) = -G \int_{\Omega(\mathbf{x}, t)} \frac{\rho(\mathbf{x}, t)}{\|\mathbf{x} - \mathbf{x}_0\|} dv \quad (3)$$

where the density  $\rho(\mathbf{x}, t)$  of the material is written in terms of the actual configuration  $\mathbf{x}$  and the time  $t$ .

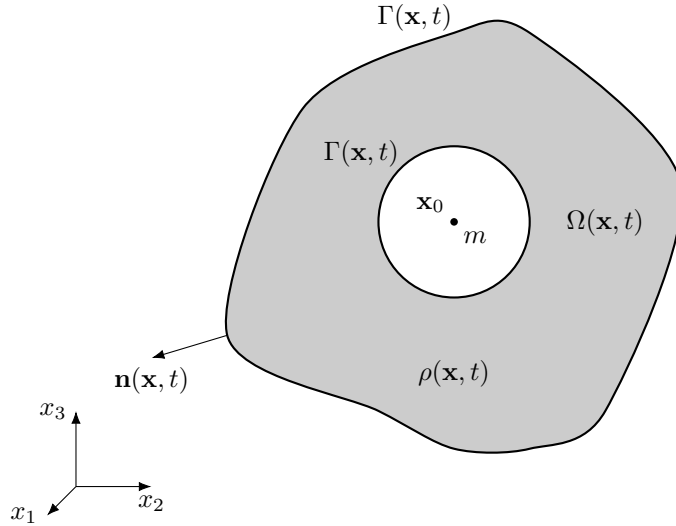


Figure 1: Point mass  $m$  at a position  $\mathbf{x}_0$  and volume  $\Omega(\mathbf{x}, t)$  with density  $\rho(\mathbf{x}, t)$ .

## 2.2. Total derivative of the gravitational potential

A seismic wave field  $\mathbf{u}(\mathbf{x}, t)$  causes density variations and, consequently, a variation of the gravitational potential  $\phi(\mathbf{x}_0, t)$ . This variation is expressed as a total derivative with respect to time:

$$\frac{D\phi(\mathbf{x}_0, t)}{Dt} = -G \frac{D}{Dt} \int_{\Omega(\mathbf{x}, t)} \frac{\rho(\mathbf{x}, t)}{\|\mathbf{x} - \mathbf{x}_0\|} dv \quad (4)$$

where it is understood that both the integrand as well as the volume  $\Omega(\mathbf{x}, t)$  depend on time  $t$ . The density  $\rho(\mathbf{x}, t)$  depends on time  $t$  due to the time dependence of the volumetric strain which results from the seismic wave field  $\mathbf{u}(\mathbf{x}, t)$ , as expressed in the conservation of mass.

The total derivative with respect to time in equation (4) is elaborated by means of Reynolds' transport theorem (Appendix A), assuming that the density  $\rho(\mathbf{x}, t)$  and the seismic wave field  $\mathbf{u}(\mathbf{x}, t)$  are continuously differentiable. Referring to equation (A.1), the scalar function  $g(\mathbf{x}, t)$  in the present case is equal to  $-G\rho(\mathbf{x}, t)/\|\mathbf{x} - \mathbf{x}_0\|$ , and the total derivative of the gravitational potential  $\Phi(\mathbf{x}_0, t)$  with respect to time is equal to:

$$\begin{aligned}
\frac{D\phi(\mathbf{x}_0, t)}{Dt} &= -G \int_{\Omega(\mathbf{x}, t)} \left[ \frac{\partial}{\partial t} \left( \frac{\rho(\mathbf{x}, t)}{\|\mathbf{x} - \mathbf{x}_0\|} \right) + \nabla \cdot \left( \frac{\rho(\mathbf{x}, t)\mathbf{v}(\mathbf{x}, t)}{\|\mathbf{x} - \mathbf{x}_0\|} \right) \right] dv \\
&= -G \int_{\Omega(\mathbf{x}, t)} \left[ \frac{\partial}{\partial t} \left( \frac{\rho(\mathbf{x}, t)}{\|\mathbf{x} - \mathbf{x}_0\|} \right) + \frac{1}{\|\mathbf{x} - \mathbf{x}_0\|} \nabla \cdot (\rho(\mathbf{x}, t)\mathbf{v}(\mathbf{x}, t)) \right. \\
&\quad \left. + \rho(\mathbf{x}, t)\mathbf{v}(\mathbf{x}, t) \cdot \nabla \frac{1}{\|\mathbf{x} - \mathbf{x}_0\|} \right] dv \\
&= -G \int_{\Omega(\mathbf{x}, t)} \left[ \frac{1}{\|\mathbf{x} - \mathbf{x}_0\|} \left( \frac{\partial \rho(\mathbf{x}, t)}{\partial t} + \mathbf{v}(\mathbf{x}, t) \cdot \nabla \rho(\mathbf{x}, t) + \rho(\mathbf{x}, t) \nabla \cdot \mathbf{v}(\mathbf{x}, t) \right) \right. \\
&\quad \left. + \rho(\mathbf{x}, t)\mathbf{v}(\mathbf{x}, t) \cdot \nabla \frac{1}{\|\mathbf{x} - \mathbf{x}_0\|} \right] dv \tag{5}
\end{aligned}$$

where  $\nabla$  denotes the gradient and  $\nabla \cdot$  the divergence. According to the conservation of mass (Appendix B), the term between round brackets in equation (5) is equal to zero. The total derivative of the gravitational potential hence reduces to:

$$\frac{D\phi(\mathbf{x}_0, t)}{Dt} = -G \int_{\Omega(\mathbf{x}, t)} \rho(\mathbf{x}, t)\mathbf{v}(\mathbf{x}, t) \cdot \nabla \frac{1}{\|\mathbf{x} - \mathbf{x}_0\|} dv \tag{6}$$

An auxiliary function  $\chi(\mathbf{x}, \mathbf{x}_0)$  is now introduced:

$$\chi(\mathbf{x}, \mathbf{x}_0) = -\nabla \frac{1}{\|\mathbf{x} - \mathbf{x}_0\|} = +\nabla_0 \frac{1}{\|\mathbf{x} - \mathbf{x}_0\|} = \frac{\mathbf{x} - \mathbf{x}_0}{\|\mathbf{x} - \mathbf{x}_0\|^3} \tag{7}$$

where  $\nabla$  and  $\nabla_0$  are the gradient operators with respect to the coordinates  $\mathbf{x}$  and  $\mathbf{x}_0$ , respectively. The total derivative of the gravitational potential is finally written as:

$$\frac{D\phi(\mathbf{x}_0, t)}{Dt} = +G \int_{\Omega(\mathbf{x}, t)} \rho(\mathbf{x}, t)\mathbf{v}(\mathbf{x}, t) \cdot \chi(\mathbf{x}, \mathbf{x}_0) dv \tag{8}$$

In equation (8), the volume  $\Omega(\mathbf{x}, t)$  can also be replaced by a fixed control volume  $\bar{\Omega}$  (Appendix A):

$$\frac{D\phi(\mathbf{x}_0, t)}{Dt} = +G \int_{\bar{\Omega}} \rho(\mathbf{x}, t)\mathbf{v}(\mathbf{x}, t) \cdot \chi(\mathbf{x}, \mathbf{x}_0) dv \tag{9}$$

An alternative formulation of the total derivative of the gravitational potential is obtained

from Reynolds' transport theorem (A.6):

$$\begin{aligned}
\frac{D\phi(\mathbf{x}_0, t)}{Dt} &= -G \int_{\Omega(\mathbf{x}, t)} \frac{\partial}{\partial t} \left( \frac{\rho(\mathbf{x}, t)}{\|\mathbf{x} - \mathbf{x}_0\|} \right) dv - G \int_{\Gamma(\mathbf{x}, t)} \frac{\rho(\mathbf{x}, t)}{\|\mathbf{x} - \mathbf{x}_0\|} \mathbf{v}(\mathbf{x}, t) \cdot \mathbf{n}(\mathbf{x}, t) da \\
&= -G \int_{\Omega(\mathbf{x}, t)} \frac{1}{\|\mathbf{x} - \mathbf{x}_0\|} \frac{\partial \rho(\mathbf{x}, t)}{\partial t} dv - G \int_{\Gamma(\mathbf{x}, t)} \frac{\rho(\mathbf{x}, t)}{\|\mathbf{x} - \mathbf{x}_0\|} \mathbf{v}(\mathbf{x}, t) \cdot \mathbf{n}(\mathbf{x}, t) da \\
&= +G \int_{\Omega(\mathbf{x}, t)} \frac{1}{\|\mathbf{x} - \mathbf{x}_0\|} \nabla \cdot (\rho(\mathbf{x}, t) \mathbf{v}(\mathbf{x}, t)) dv \\
&\quad - G \int_{\Gamma(\mathbf{x}, t)} \frac{\rho(\mathbf{x}, t)}{\|\mathbf{x} - \mathbf{x}_0\|} \mathbf{v}(\mathbf{x}, t) \cdot \mathbf{n}(\mathbf{x}, t) da \tag{10}
\end{aligned}$$

differentiating between a bulk and surface contribution. In equation (10), the volume  $\Omega(\mathbf{x}, t)$  with boundary  $\Gamma(\mathbf{x}, t)$  can also be replaced by a fixed control volume  $\bar{\Omega}$  with boundary  $\bar{\Gamma}$  (Appendix A):

$$\frac{D\phi(\mathbf{x}_0, t)}{Dt} = +G \int_{\bar{\Omega}} \frac{1}{\|\mathbf{x} - \mathbf{x}_0\|} \nabla \cdot (\rho(\mathbf{x}, t) \mathbf{v}(\mathbf{x}, t)) dv - G \int_{\bar{\Gamma}} \frac{\rho(\mathbf{x}, t)}{\|\mathbf{x} - \mathbf{x}_0\|} \mathbf{v}(\mathbf{x}, t) \cdot \mathbf{n}(\mathbf{x}, t) da \tag{11}$$

### 2.3. Variation of the gravitational potential

In a rate-independent form where the total derivative of the gravitational potential with respect to time is replaced by a variation, and the velocity vector is replaced by the displacement vector, the variation of the gravitational potential becomes:

$$\delta\phi(\mathbf{x}_0, t) = +G \int_{\bar{\Omega}} \rho(\mathbf{x}, t) \mathbf{u}(\mathbf{x}, t) \cdot \boldsymbol{\chi}(\mathbf{x}, \mathbf{x}_0) dv \tag{12}$$

This equation is equivalent to equation (43) derived by Harms [4].

Differentiating between the bulk and the surface contribution according to equation (11), the equivalent expression for the variation of the gravitational potential becomes:

$$\delta\phi(\mathbf{x}_0, t) = +G \int_{\bar{\Omega}} \frac{1}{\|\mathbf{x} - \mathbf{x}_0\|} \nabla \cdot (\rho(\mathbf{x}, t) \mathbf{u}(\mathbf{x}, t)) dv - G \int_{\bar{\Gamma}} \frac{\rho(\mathbf{x}, t)}{\|\mathbf{x} - \mathbf{x}_0\|} \mathbf{u}(\mathbf{x}, t) \cdot \mathbf{n}(\mathbf{x}, t) da \tag{13}$$

The first integral corresponds to the bulk contribution, while the second integral is the surface contribution. These expressions are equivalent to equations (46) and (47) derived by Harms [4] for a homogeneous medium.

### 2.4. Newtonian noise

The total Newtonian noise or the perturbation  $\delta\mathbf{a}_t(\mathbf{x}_0, t)$  [m/s<sup>2</sup>] is obtained as the negative gradient of the variation of the gravitational potential  $\delta\Phi(\mathbf{x}_0, t)$  with respect to the mirror position  $\mathbf{x}_0$ :

$$\delta\mathbf{a}_t(\mathbf{x}_0, t) = -\nabla_0 \delta\phi(\mathbf{x}_0, t) \tag{14}$$

Based on equation (11), the following expression is obtained for the total Newtonian noise:

$$\begin{aligned}
\delta \mathbf{a}_t(\mathbf{x}_0, t) &= -G \int_{\bar{\Omega}} \rho(\mathbf{x}, t) \nabla_0 (\mathbf{u}(\mathbf{x}, t) \cdot \boldsymbol{\chi}(\mathbf{x}, \mathbf{x}_0)) \, dv \\
&= -G \int_{\bar{\Omega}} \rho(\mathbf{x}, t) \nabla_0 \boldsymbol{\chi}(\mathbf{x}, \mathbf{x}_0) \cdot \mathbf{u}(\mathbf{x}, t) \, dv \\
&= +G \int_{\bar{\Omega}} \frac{\rho(\mathbf{x}, t)}{\|\mathbf{x} - \mathbf{x}_0\|^3} (\mathbf{I}_3 - 3\mathbf{e}_r \otimes \mathbf{e}_r) \mathbf{u}(\mathbf{x}, t) \, dv
\end{aligned} \tag{15}$$

where  $\mathbf{I}_3$  is the 3 by 3 identity matrix and the vector  $\mathbf{e}_r$  is defined as:

$$\mathbf{e}_r = \frac{\mathbf{x} - \mathbf{x}_0}{\|\mathbf{x} - \mathbf{x}_0\|} \tag{16}$$

In the frequency domain, equation (15) becomes:

$$\delta \hat{\mathbf{a}}_t(\mathbf{x}_0, \omega) = +G \int_{\bar{\Omega}} \frac{\rho(\mathbf{x})}{\|\mathbf{x} - \mathbf{x}_0\|^3} (\mathbf{I}_3 - 3\mathbf{e}_r \otimes \mathbf{e}_r) \hat{\mathbf{u}}(\mathbf{x}, \omega) \, dv \tag{17}$$

where a hat on a variable denotes its representation in the frequency domain.

Based on equation (11), the bulk and surface contribution to the total Newtonian noise can be separated:

$$\delta \mathbf{a}_t(\mathbf{x}_0, t) = \delta \mathbf{a}_b(\mathbf{x}_0, t) + \delta \mathbf{a}_s(\mathbf{x}_0, t) \tag{18}$$

where the bulk contribution  $\delta \mathbf{a}_b(\mathbf{x}_0, t)$  is equal to:

$$\delta \mathbf{a}_b(\mathbf{x}_0, t) = -G \int_{\bar{\Omega}} \boldsymbol{\chi}(\mathbf{x}, \mathbf{x}_0) \nabla \cdot (\rho(\mathbf{x}, t) \mathbf{u}(\mathbf{x}, t)) \, dv \tag{19}$$

and the surface contribution  $\delta \mathbf{a}_s(\mathbf{x}_0, t)$  is equal to:

$$\delta \mathbf{a}_s(\mathbf{x}_0, t) = +G \int_{\Gamma} \boldsymbol{\chi}(\mathbf{x}, \mathbf{x}_0) \rho(\mathbf{x}, t) \mathbf{u}(\mathbf{x}, t) \cdot \mathbf{n}(\mathbf{x}, t) \, da \tag{20}$$

In the frequency domain, the bulk contribution  $\delta \hat{\mathbf{a}}_b(\mathbf{x}_0, \omega)$  is equal to:

$$\delta \hat{\mathbf{a}}_b(\mathbf{x}_0, \omega) = -G \int_{\bar{\Omega}} \boldsymbol{\chi}(\mathbf{x}, \mathbf{x}_0) \nabla \cdot (\rho(\mathbf{x}) \hat{\mathbf{u}}(\mathbf{x}, \omega)) \, dv \tag{21}$$

while the surface contribution  $\delta \hat{\mathbf{a}}_s(\mathbf{x}_0, \omega)$  is equal to:

$$\delta \hat{\mathbf{a}}_s(\mathbf{x}_0, \omega) = +G \int_{\Gamma} \boldsymbol{\chi}(\mathbf{x}, \mathbf{x}_0) \rho(\mathbf{x}) \hat{\mathbf{u}}(\mathbf{x}, \omega) \cdot \mathbf{n}(\mathbf{x}) \, da \tag{22}$$

### 3. Finite element formulation

#### 3.1. Total Newtonian noise

In order to evaluate the volume integral in equation (17), the control volume  $\bar{\Omega}$  is discretized into  $n_e$  finite elements (FE) with volume  $\bar{\Omega}^e$  and constant density  $\rho_e$ , resulting in the following sum:

$$\delta \hat{\mathbf{a}}_t(\mathbf{x}_0, \omega) \simeq \sum_{e=1}^{n_e} G \int_{\bar{\Omega}^e} \frac{\rho_e}{\|\mathbf{x} - \mathbf{x}_0\|^3} (\mathbf{I}_3 - 3\mathbf{e}_r \otimes \mathbf{e}_r) \hat{\mathbf{u}}^e(\mathbf{x}, \omega) dv \quad (23)$$

where  $\hat{\mathbf{u}}^e(\mathbf{x}, \omega)$  are the element displacements.

The element displacements  $\hat{\mathbf{u}}^e(\boldsymbol{\xi}, \omega)$  in the local coordinate system are approximated using the shape functions  $N_k^e(\boldsymbol{\xi})$

$$\hat{\mathbf{u}}^e(\boldsymbol{\xi}, \omega) \simeq \sum_{k=1}^n \mathbf{N}_k^e(\boldsymbol{\xi}) \hat{\mathbf{u}}_k^e = \mathbf{N}^e(\boldsymbol{\xi}) \hat{\mathbf{u}}^e \quad (24)$$

where  $\hat{\mathbf{u}}^e = \{\hat{\mathbf{u}}_1^{eT}, \hat{\mathbf{u}}_2^{eT}, \dots, \hat{\mathbf{u}}_n^{eT}\}^T$  is a column vector containing the nodal values of  $\hat{\mathbf{u}}^e(\boldsymbol{\xi}, \omega)$  and  $\mathbf{N}^e(\boldsymbol{\xi}) = [\mathbf{N}_1^e(\boldsymbol{\xi}), \mathbf{N}_2^e(\boldsymbol{\xi}), \dots, \mathbf{N}_n^e(\boldsymbol{\xi})]$ . Within each element, an isoparametric transformation is employed to transform the global coordinate  $\mathbf{x} = \{x_1, x_2, x_3\}^T$  to a local (element) coordinate  $\boldsymbol{\xi} = \{\xi_1, \xi_2, \xi_3\}^T$  using shape functions  $N_k^e(\boldsymbol{\xi})$ :

$$\mathbf{x}(\boldsymbol{\xi}) = \sum_{k=1}^n \begin{bmatrix} N_k^e(\boldsymbol{\xi}) & 0 & 0 \\ 0 & N_k^e(\boldsymbol{\xi}) & 0 \\ 0 & 0 & N_k^e(\boldsymbol{\xi}) \end{bmatrix} \mathbf{x}_k = \sum_{k=1}^n \mathbf{N}_k^e(\boldsymbol{\xi}) \mathbf{x}_k \quad (25)$$

where  $n$  is the number of nodes in the element and  $\mathbf{x}_k$  is the global coordinate of node  $k$ . The integral in equation (23) over the volume  $\bar{\Omega}^e$  of each element is subsequently transformed to the local coordinate  $\boldsymbol{\xi}$ :

$$dv = \det(\mathbf{J}^e(\boldsymbol{\xi})) d\xi_1 d\xi_2 d\xi_3 \quad (26)$$

where the Jacobian  $\mathbf{J}^e(\boldsymbol{\xi})$  is defined as:

$$\mathbf{J}^e(\boldsymbol{\xi}) = \begin{bmatrix} \frac{\partial x_1}{\partial \xi_1} & \frac{\partial x_2}{\partial \xi_1} & \frac{\partial x_3}{\partial \xi_1} \\ \frac{\partial x_1}{\partial \xi_2} & \frac{\partial x_2}{\partial \xi_2} & \frac{\partial x_3}{\partial \xi_2} \\ \frac{\partial x_1}{\partial \xi_3} & \frac{\partial x_2}{\partial \xi_3} & \frac{\partial x_3}{\partial \xi_3} \end{bmatrix} = \sum_{k=1}^n \begin{bmatrix} \frac{\partial N_k^e(\boldsymbol{\xi})}{\partial \xi_1} x_{k1} & \frac{\partial N_k^e(\boldsymbol{\xi})}{\partial \xi_1} x_{k2} & \frac{\partial N_k^e(\boldsymbol{\xi})}{\partial \xi_1} x_{k3} \\ \frac{\partial N_k^e(\boldsymbol{\xi})}{\partial \xi_2} x_{k1} & \frac{\partial N_k^e(\boldsymbol{\xi})}{\partial \xi_2} x_{k2} & \frac{\partial N_k^e(\boldsymbol{\xi})}{\partial \xi_2} x_{k3} \\ \frac{\partial N_k^e(\boldsymbol{\xi})}{\partial \xi_3} x_{k1} & \frac{\partial N_k^e(\boldsymbol{\xi})}{\partial \xi_3} x_{k2} & \frac{\partial N_k^e(\boldsymbol{\xi})}{\partial \xi_3} x_{k3} \end{bmatrix} \quad (27)$$

using the isoparametric transformation (25). Substituting equation (26) into equation (23), the volume integral is expressed in the local coordinate system:

$$\delta \hat{\mathbf{a}}_t(\mathbf{x}_0, \omega) \simeq \sum_{e=1}^{n_e} G \int_{-1}^{+1} \int_{-1}^{+1} \int_{-1}^{+1} \frac{\rho_e}{\|\mathbf{x} - \mathbf{x}_0\|^3} (\mathbf{I}_3 - 3\mathbf{e}_r \otimes \mathbf{e}_r) \hat{\mathbf{u}}^e(\boldsymbol{\xi}, \omega) \det(\mathbf{J}^e(\boldsymbol{\xi})) d\xi_1 d\xi_2 d\xi_3 \quad (28)$$

where the explicit dependence of the coordinate  $\mathbf{x}$  on the local coordinate  $\boldsymbol{\xi}$  (equation (25)) is omitted for brevity. Substituting the approximation (24) of the displacement field and factoring the element displacement vector  $\hat{\mathbf{u}}^e$  results in the following:

$$\delta \hat{\mathbf{a}}_t(\mathbf{x}_0, \omega) \simeq \sum_{e=1}^{n_e} \left[ G \int_{-1}^{+1} \int_{-1}^{+1} \int_{-1}^{+1} \frac{\rho_e}{\|\mathbf{x} - \mathbf{x}_0\|^3} (\mathbf{I}_3 - 3\mathbf{e}_r \otimes \mathbf{e}_r) \mathbf{N}^e(\boldsymbol{\xi}) \det(\mathbf{J}^e(\boldsymbol{\xi})) d\xi_1 d\xi_2 d\xi_3 \right] \hat{\mathbf{u}}^e \quad (29)$$

The unit vector  $\mathbf{e}_r$  depends on the coordinate  $\mathbf{x}$  and, hence, also on the local coordinate  $\boldsymbol{\xi}$ . The integrals are evaluated using Gaussian quadrature with  $n_G$  Gauss points with local coordinates  $\boldsymbol{\xi}_j$  and the corresponding weights  $w_j$ , resulting in the following:

$$\begin{aligned} \delta \hat{\mathbf{a}}_t(\mathbf{x}_0, \omega) &\simeq \sum_{e=1}^{n_e} \left[ G \sum_{j=1}^{n_G} w_j \frac{\rho_e}{\|\mathbf{x}_j - \mathbf{x}_0\|^3} (\mathbf{I}_3 - 3\mathbf{e}_r \otimes \mathbf{e}_r) \mathbf{N}^e(\boldsymbol{\xi}_j) \det(\mathbf{J}^e(\boldsymbol{\xi}_j)) \right] \hat{\mathbf{u}}^e \\ &= \sum_{e=1}^{n_e} \mathbf{A}_t^e \hat{\mathbf{u}}^e \end{aligned} \quad (30)$$

where  $\mathbf{x}_j = \mathbf{x}(\boldsymbol{\xi}_j)$  is the global coordinate of the Gauss point  $j$ . The matrix  $\mathbf{A}_t^e$  of dimension  $3 \times 3n$  yields the contribution of the nodal displacements  $\hat{\mathbf{u}}^e$  of element  $e$  to the total Newtonian noise. The element matrices  $\mathbf{A}_t^e$  are assembled into a global matrix  $\mathbf{A}_t$  of dimension  $3 \times 3N$ , with  $N$  the number of nodes in the volume  $\bar{\Omega}$ , yielding:

$$\delta \hat{\mathbf{a}}_t(\mathbf{x}_0, \omega) = \mathbf{A}_t \hat{\mathbf{u}}(\omega) \quad (31)$$

The displacement vector  $\hat{\mathbf{u}}(\omega)$  contains the nodal values of the seismic wave field in the volume  $\bar{\Omega}$ . As the matrix  $\mathbf{A}_t$  does not depend on the seismic wave field  $\hat{\mathbf{u}}(\mathbf{x}, \omega)$ , it only needs to be computed once for a particular soil layering and cavity geometry. The computation of the total Newtonian noise hence reduces to a matrix-vector multiplication for a particular seismic wave field.

### 3.2. Bulk contribution to the Newtonian noise

The bulk contribution to the Newtonian noise  $\delta \hat{\mathbf{a}}_b(\mathbf{x}_0, \omega)$ , as defined in equation (21), is approximated as follows with a finite element formulation:

$$\delta \hat{\mathbf{a}}_b(\mathbf{x}_0, \omega) \simeq \sum_{e=1}^{n_e} -G \int_{\bar{\Omega}^e} \rho_e \boldsymbol{\chi}(\mathbf{x}, \mathbf{x}_0) \nabla \cdot \hat{\mathbf{u}}^e(\mathbf{x}, \omega) dv \quad (32)$$

Substituting equations (24) and (26) gives:

$$\delta \hat{\mathbf{a}}_b(\mathbf{x}_0, \omega) \simeq \sum_{e=1}^{n_e} \left[ -G \int_{-1}^{+1} \int_{-1}^{+1} \int_{-1}^{+1} \rho_e \boldsymbol{\chi}(\mathbf{x}, \mathbf{x}_0) \mathbf{B}^e(\boldsymbol{\xi}) \det(\mathbf{J}^e(\boldsymbol{\xi})) d\xi_1 d\xi_2 d\xi_3 \right] \hat{\mathbf{u}}^e \quad (33)$$

where the explicit dependence of the coordinate  $\mathbf{x}$  on the local coordinate  $\boldsymbol{\xi}$  is omitted for brevity and the row vector  $\mathbf{B}^e(\boldsymbol{\xi})$  of dimension  $1 \times 3n$  contains the derivatives of the shape functions  $N_k^e(\boldsymbol{\xi})$  with respect to the global coordinates  $\mathbf{x}$ :

$$\mathbf{B}^e(\boldsymbol{\xi}) = \left\{ \frac{\partial N_1^e(\boldsymbol{\xi})}{\partial x_1} \quad \frac{\partial N_1^e(\boldsymbol{\xi})}{\partial x_2} \quad \frac{\partial N_1^e(\boldsymbol{\xi})}{\partial x_3} \quad \frac{\partial N_2^e(\boldsymbol{\xi})}{\partial x_1} \quad \dots \quad \frac{\partial N_n^e(\boldsymbol{\xi})}{\partial x_3} \right\} \quad (34)$$

These derivatives are computed using the inverse of the Jacobian matrix  $\mathbf{J}^e(\boldsymbol{\xi})$ :

$$\left\{ \begin{array}{c} \frac{\partial N_k^e(\boldsymbol{\xi})}{\partial x_1} \\ \frac{\partial N_k^e(\boldsymbol{\xi})}{\partial x_2} \\ \frac{\partial N_k^e(\boldsymbol{\xi})}{\partial x_3} \end{array} \right\} = \mathbf{J}^e(\boldsymbol{\xi})^{-1} \left\{ \begin{array}{c} \frac{\partial N_k^e(\boldsymbol{\xi})}{\partial \xi_1} \\ \frac{\partial N_k^e(\boldsymbol{\xi})}{\partial \xi_2} \\ \frac{\partial N_k^e(\boldsymbol{\xi})}{\partial \xi_3} \end{array} \right\} \quad (35)$$

Gaussian quadrature is applied to evaluate the volume integral in the local coordinate system:

$$\delta \hat{\mathbf{a}}_b(\mathbf{x}_0, \omega) \simeq \sum_{e=1}^{n_e} \left[ -G \sum_{j=1}^{n_G} w_j \rho_e \boldsymbol{\chi}(\mathbf{x}_j, \mathbf{x}_0) \mathbf{B}^e(\boldsymbol{\xi}_j) \det(\mathbf{J}^e(\boldsymbol{\xi}_j)) \right] \hat{\mathbf{u}}^e = \sum_{e=1}^{n_e} \mathbf{A}_b^e \hat{\mathbf{u}}^e \quad (36)$$

Assembling the matrix  $\mathbf{A}_b$  of dimension  $3 \times 3N$  that accounts for the contribution of all elements yields:

$$\delta \hat{\mathbf{a}}_b(\mathbf{x}_0, \omega) = \mathbf{A}_b \hat{\mathbf{u}}(\omega) \quad (37)$$

The bulk contribution to the Newtonian noise can be computed as a matrix-vector multiplication for a particular seismic wave field  $\hat{\mathbf{u}}(\omega)$ .

### 3.3. Surface contribution to the Newtonian Noise

The surface contribution to the Newtonian Noise  $\delta \hat{\mathbf{a}}_s(\mathbf{x}_0, \omega)$ , as defined in equation (22), is computed by considering the surface  $\bar{\Gamma}^e$  of each finite element with volume  $\bar{\Omega}^e$  individually and adding the contribution of all elements:

$$\delta \hat{\mathbf{a}}_s(\mathbf{x}_0, \omega) \simeq \sum_{e=1}^{n_e} G \int_{\bar{\Gamma}^e} \rho_e \boldsymbol{\chi}(\mathbf{x}, \mathbf{x}_0) \hat{\mathbf{u}}^e(\mathbf{x}, \omega) \cdot \mathbf{n}^e(\mathbf{x}) da \quad (38)$$

The contribution of a shared surface between two neighboring finite elements with identical density  $\rho_e$  cancels as the unit outward normal vectors  $\mathbf{n}^e(\mathbf{x})$  on both surfaces point in opposite directions. However, if the density varies from one element to another, this results in a contribution to the Newtonian noise that is proportional to the difference in density.

The surface  $\bar{\Gamma}^e$  of element  $e$  is subdivided in  $n_s$  faces (e.g.  $n_s = 4$  for tetrahedral elements and  $n_s = 6$  for brick elements). Equation (38) is rewritten as follows:

$$\delta \hat{\mathbf{a}}_s(\mathbf{x}_0, \omega) \simeq \sum_{e=1}^{n_e} \sum_{l=1}^{n_s} G \int_{\bar{\Gamma}_l^e} \rho_e \boldsymbol{\chi}(\mathbf{x}, \mathbf{x}_0) \hat{\mathbf{u}}_l^e(\mathbf{x}, \omega) \cdot \mathbf{n}_l^e(\mathbf{x}) da \quad (39)$$

where  $\bar{\Gamma}_l^e$  denotes the surface of the face  $l$  belonging to element  $e$ , and  $\hat{\mathbf{u}}_l^e(\mathbf{x}, \omega)$  and  $\mathbf{n}_l^e(\mathbf{x})$  the corresponding displacement vector and unit outward normal vector. The displacements  $\hat{\mathbf{u}}_l^e(\mathbf{x}, \omega)$  are approximated using shape functions  $\mathbf{N}^e(\boldsymbol{\eta})$ , where the isoparametric transformation for surface integrals is performed from the global coordinate  $\mathbf{x}$  to the local coordinate  $\boldsymbol{\eta} = \{\eta_1, \eta_2\}^T$ :

$$\hat{\mathbf{u}}_l^e(\boldsymbol{\eta}, \omega) \simeq \sum_{k=1}^n \mathbf{N}_k^e(\boldsymbol{\eta}) \hat{\mathbf{u}}_{lk}^e = \mathbf{N}^e(\boldsymbol{\eta}) \hat{\mathbf{u}}_l^e \quad (40)$$

and  $n$  is the number of nodes on the surface  $\bar{\Gamma}_l^e$ . The Jacobian  $\mathbf{J}^e(\boldsymbol{\eta})$  for this isoparametric transformation is the following  $2 \times 3$  matrix:

$$\mathbf{J}^e(\boldsymbol{\eta}) = \begin{bmatrix} \frac{\partial \mathbf{x}}{\partial \eta_1} \\ \frac{\partial \mathbf{x}}{\partial \eta_2} \end{bmatrix} = \begin{bmatrix} \frac{\partial N_k^e(\boldsymbol{\eta})}{\partial \eta_1} x_{k1} & \frac{\partial N_k^e(\boldsymbol{\eta})}{\partial \eta_1} x_{k2} & \frac{\partial N_k^e(\boldsymbol{\eta})}{\partial \eta_1} x_{k3} \\ \frac{\partial N_k^e(\boldsymbol{\eta})}{\partial \eta_2} x_{k1} & \frac{\partial N_k^e(\boldsymbol{\eta})}{\partial \eta_2} x_{k2} & \frac{\partial N_k^e(\boldsymbol{\eta})}{\partial \eta_2} x_{k3} \end{bmatrix} = \begin{bmatrix} \mathbf{j}_1(\boldsymbol{\eta}) \\ \mathbf{j}_2(\boldsymbol{\eta}) \end{bmatrix} \quad (41)$$

The surface integral over  $\bar{\Gamma}_l^e$  in equation (39) is transformed to the local coordinate  $\boldsymbol{\eta}$  using the following expression for the infinitesimal area  $da$ :

$$da = \|\mathbf{j}_1(\boldsymbol{\eta}) \times \mathbf{j}_2(\boldsymbol{\eta})\| d\eta_1 d\eta_2 \quad (42)$$

Substituting expressions (40) and (42) into equation (39) yields:

$$\delta \hat{\mathbf{a}}_s(\mathbf{x}_0, \omega) \simeq \sum_{e=1}^{n_e} \sum_{l=1}^{n_s} \left[ G \int_{-1}^{+1} \int_{-1}^{+1} \rho_e \chi(\mathbf{x}, \mathbf{x}_0) \mathbf{n}_l^e(\mathbf{x}) \mathbf{N}^e(\boldsymbol{\eta}) \|\mathbf{j}_1(\boldsymbol{\eta}) \times \mathbf{j}_2(\boldsymbol{\eta})\| d\eta_1 d\eta_2 \right] \hat{\mathbf{u}}_l^e \quad (43)$$

where the explicit dependence of  $\mathbf{x}$  on  $\boldsymbol{\eta}$  is omitted for brevity. Gaussian quadrature is applied to evaluate the surface integral in the local coordinate system using  $n_G$  Gauss points for each face  $l$ :

$$\begin{aligned} \delta \hat{\mathbf{a}}_s(\mathbf{x}_0, \omega) &\simeq \sum_{e=1}^{n_e} \sum_{l=1}^{n_s} \left[ G \sum_{j=1}^{n_G} w_j \rho_e \chi(\mathbf{x}_j, \mathbf{x}_0) \mathbf{n}_l^e(\mathbf{x}_j) \mathbf{N}^e(\boldsymbol{\eta}_j) \|\mathbf{j}_1(\boldsymbol{\eta}_j) \times \mathbf{j}_2(\boldsymbol{\eta}_j)\| \right] \hat{\mathbf{u}}_l^e \\ &= \sum_{e=1}^{n_e} \sum_{l=1}^{n_s} \mathbf{A}_{sl}^e \hat{\mathbf{u}}_l^e \\ &= \sum_{e=1}^{n_e} \mathbf{A}_s^e \hat{\mathbf{u}}^e \end{aligned} \quad (44)$$

$\mathbf{x}_j = \mathbf{x}(\boldsymbol{\eta}_j)$  is the global coordinate of the Gauss point  $j$ . Assembling the global matrix  $\mathbf{A}_s$  of dimension  $3 \times 3N$  to account for the contribution of all elements yields:

$$\delta \hat{\mathbf{a}}_s(\mathbf{x}_0, \omega) = \mathbf{A}_s \hat{\mathbf{u}}(\omega) \quad (45)$$

The contribution of a particular part of the surface  $\bar{\Gamma}$  can be evaluated by selecting the corresponding degrees of freedom of the nodal displacement vector  $\hat{\mathbf{u}}(\omega)$  and the matrix  $\mathbf{A}_s$ .

### 3.4. Implementation

The finite element computation of the Newtonian noise is implemented in the **ANNA Newtonian Noise Analysis** toolbox within the MATLAB programming and numeric computing platform, making use of subroutines embedded in Stabil, an educational MATLAB toolbox for static and dynamic structural analysis [21]. ANNA is compatible with the open-source GNU Octave Scientific Programming Language [22], while a Python version is also available.

The Newtonian noise is computed for a seismic wave field that is defined on a 3D finite element mesh. The toolbox in its present form supports linear (4-node) and quadratic (10-node) tetrahedral finite elements, as well as linear (8-node) and quadratic (20-node) brick finite elements.

At the core of ANNA is a dedicated subroutine `asmnn.m` that takes the 3D finite element mesh and material properties (density) as input and computes the finite element matrices  $\mathbf{A}_t$ ,  $\mathbf{A}_b$  and  $\mathbf{A}_s$  of dimension  $3 \times 3N$ , with  $N$  the number of nodes in the finite element mesh.

### 3.5. Work flow

The computation of Newtonian noise hence reduces to the following four-step procedure:

1. Create a 3D finite element mesh which an extension and refinement that is tailored to well represent the seismic wave field in the frequency range of interest, as well as the function  $\chi(\mathbf{x}, \mathbf{x}_0)$  and its gradient, so that Newtonian noise can be computed with good accuracy. This will be explained in detail when presenting the verification examples in section 4. We use Gmsh [23] to create 3D finite element meshes with  $N$  nodes and  $3N$  degrees of freedom.
2. Compute a 3D seismic wave field, stored as a column vector  $\hat{\mathbf{u}}(\omega)$  of dimension  $3N \times 1$ , where each entry corresponds to a degree of freedom of the  $N$  nodes of a finite element mesh. As mentioned in the introduction, a wide variety of methods and tools with different degree of complexity can be used to compute the seismic wave field. If the cost to compute the seismic wave field is high, it can be computed on a coarser finite element mesh than the one that is finally used to compute the Newtonian noise (which may need to be fine due to the discretization of the function  $\chi(\mathbf{x}, \mathbf{x}_0)$  and its gradient); in this case, an additional step is needed where the seismic wave field is interpolated on the finer mesh.
3. Use the subroutine `asmnn.m` in ANNA to compute the finite element matrices  $\mathbf{A}_t$ ,  $\mathbf{A}_b$  and  $\mathbf{A}_s$  of dimension  $3 \times 3N$ , based on the 3D finite element mesh and material properties (density).
4. Compute the total Newtonian noise  $\delta\hat{\mathbf{a}}_t(\mathbf{x}_0, \omega)$  according to equation (31) as the product of the finite element matrix  $\mathbf{A}_t$  and the displacement vector  $\hat{\mathbf{u}}(\omega)$ , resulting in a column vector of dimension  $3 \times 1$ . Similarly, the bulk and surface contributions  $\delta\hat{\mathbf{a}}_b(\mathbf{x}_0, \omega)$  and  $\delta\hat{\mathbf{a}}_s(\mathbf{x}_0, \omega)$  are computed according to equations (37) and (45) as the product of the finite element matrices  $\mathbf{A}_b$  and  $\mathbf{A}_s$  and the displacement vector  $\hat{\mathbf{u}}(\omega)$ .

## 4. Verification

The resulting numerical formulation, as implemented in the **ANNA Newtonian Noise Analysis** toolbox, is verified using available analytical solutions for Newtonian noise [4]. Three configurations are considered. First, plane harmonic P- and S-waves propagating in a homogeneous linear elastic full space with a cavity with radius  $r_0$  are examined. Next, Rayleigh waves propagating along the surface of a homogeneous linear elastic halfspace are considered, and the Newtonian Noise on a test mass at a distance  $h$  above the free surface is computed.

### 4.1. Plane harmonic P-wave in a full space

First, a mirror suspended in a spherical cavity with radius  $r_0$  at the center  $\mathbf{x}_0 = \{0, 0, 0\}^T$  of an homogeneous linear elastic full space  $\Omega$  is considered. Newtonian noise is computed for a plane harmonic P-wave with a wavelength  $\lambda_p$  that – in the low frequency range considered – is assumed to be much larger than the cavity radius  $r_0$ , so that wave scattering due to the cavity can be ignored.

The displacement vector  $\hat{\mathbf{u}}(\mathbf{x}, \omega)$  due to a plane harmonic P-wave with unit amplitude propagating with velocity  $C_p$  in the direction  $\mathbf{e}_k$  is equal to:

$$\hat{\mathbf{u}}(\mathbf{x}, \omega) = \exp(-ik_p \mathbf{e}_k \cdot \mathbf{x}) \mathbf{e}_k \quad (46)$$

where  $k_p = \omega/C_p = 2\pi/\lambda_p$  is the longitudinal wavenumber and  $\omega$  is the circular frequency.

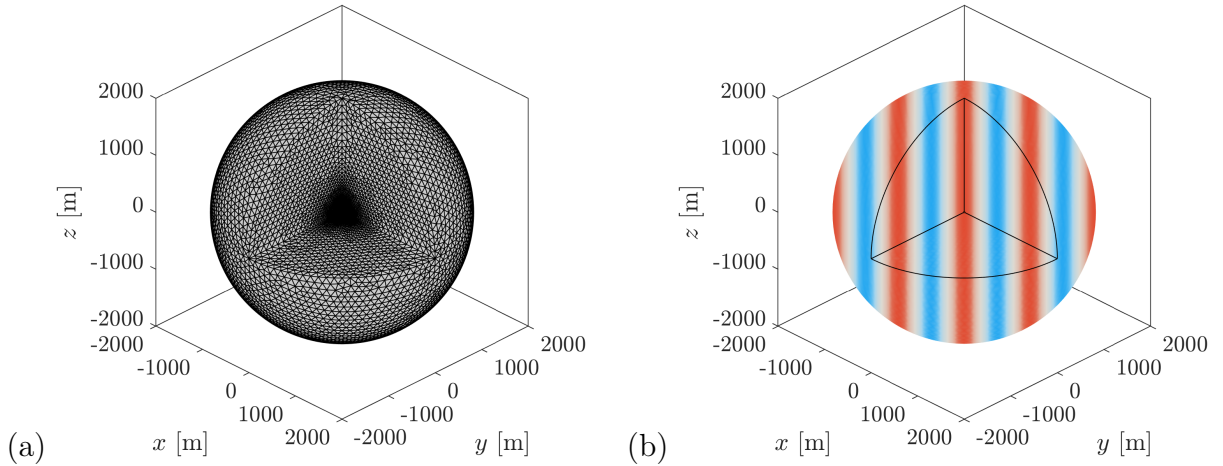


Figure 2: (a) Finite element mesh of a sphere with center at  $\mathbf{x}_0 = \{0, 0, 0\}^T$  and radius  $R = 2000$  m and a spherical cavity with radius  $r_0 = 20$  m, used to compute the Newtonian noise due to a plane harmonic P-wave in a frequency range around 5 Hz. (b) Displacement  $\hat{u}_x(\mathbf{x}, \omega)$  due to a plane harmonic P-wave with unit amplitude and frequency of 5 Hz, propagating in the direction  $\mathbf{e}_k = \{\frac{1}{\sqrt{2}}, \frac{1}{\sqrt{2}}, 0\}^T$ .

Figure 2b shows the displacement component  $\hat{u}_x(\mathbf{x}, \omega)$  of a plane harmonic P-wave with unit amplitude and frequency of 5 Hz, propagating in the direction  $\mathbf{e}_k = \{\frac{1}{\sqrt{2}}, \frac{1}{\sqrt{2}}, 0\}^T$  in a homogeneous linear elastic full space with shear wave velocity  $C_s = 2500$  m/s, dilatational wave velocity  $C_p = 5000$  m/s, and density  $\rho = 2800$  kg/m<sup>3</sup>; the wave field is shown on a

spherical finite element mesh that will subsequently be used to compute the Newtonian noise. Since the displacement  $\hat{u}_y(\mathbf{x}, \omega)$  is equal to  $\hat{u}_x(\mathbf{x}, \omega)$ , while  $\hat{u}_z(\mathbf{x}, \omega)$  is zero, these components are not shown. The wavelength  $\lambda_p = 1000$  m at 5 Hz is much larger than the cavity radius  $r_0 = 20$  m, so that wave scattering by the cavity indeed can be disregarded.

For a plane harmonic P-wave propagating in a linear elastic full space, an analytical expression for the Newtonian noise can be derived if wave scattering by the cavity is ignored. Inserting equation (46) into equation (17) and evaluating the volume integral in spherical coordinates between radii  $r_0$  and  $R$  yields the following analytical expression for the Newtonian noise  $\delta\hat{\mathbf{a}}_t(\mathbf{x}_0, \omega)$  at the mirror position  $\mathbf{x}_0$  [4]:

$$\delta\hat{\mathbf{a}}_t(\mathbf{x}_0, \omega) = 8\pi\rho G \left( \frac{j_1(k_p r_0)}{k_p r_0} - \frac{j_1(k_p R)}{k_p R} \right) \hat{\mathbf{u}}(\mathbf{x}_0, \omega) \quad (47)$$

where  $j_1(\cdot)$  is the spherical Bessel function of the first kind and order 1. Assuming a full space, taking the limit for  $R \rightarrow \infty$  yields:

$$\delta\hat{\mathbf{a}}_t(\mathbf{x}_0, \omega) = 8\pi\rho G \frac{j_1(k_p r_0)}{k_p r_0} \hat{\mathbf{u}}(\mathbf{x}_0, \omega) \quad (48)$$

The analytical solution for the bulk contribution  $\delta\hat{\mathbf{a}}_b(\mathbf{x}_0, \omega)$  is

$$\delta\hat{\mathbf{a}}_b(\mathbf{x}_0, \omega) = 4\pi\rho G (j_0(k_p r_0) - j_0(k_p R)) \hat{\mathbf{u}}(\mathbf{x}_0, \omega) \quad (49)$$

and, for a full space, the corresponding limit for  $R \rightarrow \infty$  is:

$$\delta\hat{\mathbf{a}}_b(\mathbf{x}_0, \omega) = 4\pi\rho G j_0(k_p r_0) \hat{\mathbf{u}}(\mathbf{x}_0, \omega) \quad (50)$$

Similarly, the analytical solution for the surface contribution  $\delta\hat{\mathbf{a}}_s(\mathbf{x}_0, \omega)$  is:

$$\delta\hat{\mathbf{a}}_s(\mathbf{x}_0, \omega) = 8\pi\rho G \left( \frac{j_1(k_p r_0)}{k_p r_0} - \frac{1}{2}j_0(k_p r_0) - \frac{j_1(k_p R)}{k_p R} + \frac{1}{2}j_0(k_p R) \right) \hat{\mathbf{u}}(\mathbf{x}_0, \omega), \quad (51)$$

while its full space limit is given by:

$$\delta\hat{\mathbf{a}}_s(\mathbf{x}_0, \omega) = 8\pi\rho G \left( \frac{j_1(k_p r_0)}{k_p r_0} - \frac{1}{2}j_0(k_p r_0) \right) \hat{\mathbf{u}}(\mathbf{x}_0, \omega). \quad (52)$$

The Newtonian noise is subsequently evaluated with the ANNA toolbox using the finite element formulation presented in section 3. A finite element mesh is constructed on a spherical domain with center at  $\mathbf{x}_0$  and radius  $R$  for calculations in the frequency range  $f \in [f_{\min}, f_{\max}]$ , where  $f$  is equal to  $\omega/(2\pi)$ , taking into consideration the following three criteria:

1. The radius  $R$  of the spherical finite element domain must be sufficiently large in order to well incorporate the far field contributions to the Newtonian noise for all frequencies  $f \in [f_{\min}, f_{\max}]$ .

The truncation error  $\Delta_t(R, \omega)$  on the total Newtonian noise  $\delta \hat{\mathbf{a}}_t(\mathbf{x}_0, \omega)$  for a spherical domain with radius  $R$  is obtained by subtracting equation (47) from equation (48):

$$\Delta_t(R, \omega) = +8\pi\rho G \frac{j_1(k_p R)}{k_p R} \hat{\mathbf{u}}(\mathbf{x}_0, \omega) \quad (53)$$

This truncation error is governed by the factor  $|j_1(k_p R)/(k_p R)|$ , which is limited to a tolerance  $\varepsilon$  at the lowest frequency  $f_{\min}$ :

$$\left| \frac{j_1(k_p R)}{k_p R} \right| \leq \varepsilon \quad \text{for } f = f_{\min}. \quad (54)$$

For a tolerance  $\varepsilon = 0.01$ , a radius  $R \gtrsim 1.7\lambda_p^{\max}$  is required.

The truncation error  $\Delta_b(R, \omega)$  on the bulk contribution is equal to:

$$\Delta_b(R, \omega) = -4\pi\rho G j_0(k_p R) \hat{\mathbf{u}}(\mathbf{x}_0, \omega). \quad (55)$$

and a tolerance  $\varepsilon$  can again be imposed on the factor depending on  $k_p R$ :

$$|j_0(k_p R)| \leq \varepsilon \quad \text{for } f = f_{\min}. \quad (56)$$

The truncation error  $\Delta_s(R, \omega)$  on the surface contribution is equal to:

$$\Delta_s(R, \omega) = +4\pi\rho G \left( j_0(k_p R) - 2 \frac{j_1(k_p R)}{k_p R} \right) \hat{\mathbf{u}}(\mathbf{x}_0, \omega). \quad (57)$$

and a tolerance  $\varepsilon$  can be imposed on the factor depending on  $k_p R$ :

$$\left| j_0(k_p R) - 2 \frac{j_1(k_p R)}{k_p R} \right| \leq \varepsilon \quad \text{for } f = f_{\min}. \quad (58)$$

As the truncation errors  $\Delta_b(R, \omega)$  and  $\Delta_s(R, \omega)$  decay more slowly with  $R$  than the truncation error  $\Delta_t(R, \omega)$ , enforcing a similar tolerance  $\varepsilon = 0.01$  in equations (56) and (58) would require a substantially larger domain with radius  $R \gtrsim 15.9\lambda_p^{\max}$  for the bulk contribution and  $R \gtrsim 16.2\lambda_p^{\max}$  for the surface contribution.

2. The element size  $l_e$  should be sufficiently small to well resolve the propagating waves. It is therefore limited to  $l_e^{\min} = \lambda^{\min}/n$ , with  $\lambda^{\min}$  the smallest wavelength and  $n$  the number of finite elements per wavelength.
3. The finite element mesh is refined near the cavity to accurately resolve the strong spatial variation of the function  $\chi(\mathbf{x}, \mathbf{x}_0)$  in equations (21) and (22) and its gradient in equation (17). Since this function contains the factor  $1/\|\mathbf{x} - \mathbf{x}_0\|^3$ , its magnitude

increases rapidly as the distance  $r = \|\mathbf{x} - \mathbf{x}_0\|$  from the cavity decreases, which determines mesh refinement close to the cavity. To obtain a practical estimate, the relative variation of the function  $f(r) = 1/r^3$  is evaluated across an element of size  $l_e(r)$  at a distance  $r$ . A first-order approximation gives:

$$\frac{\Delta f}{f} \approx \frac{|f'(r)|}{f(r)} l_e(r) = \frac{3}{r} l_e(r). \quad (59)$$

Imposing a tolerance  $\eta$  on this variation leads to the condition:

$$l_e(r) \leq \frac{\eta}{3} r. \quad (60)$$

Evaluated on the surface of the cavity  $r = r_0$ , this yields a minimum element size  $l_{e0} = \eta r_0/3$ . The mesh is then graded according to a power law:

$$l_e(r) = l_{e0} \left( \frac{r}{r_0} \right)^\alpha, \quad (61)$$

so that the element size  $l_e(r)$  increases smoothly with distance  $r$  from the cavity. This grading is applied until the element size  $l_e^{\min}$  imposed by the second criterion is reached, beyond which the element size is kept constant.

Figure 2a shows the finite element mesh that is used for the numerical computation of the Newtonian noise due to a plane harmonic P-wave or S-wave. This finite element mesh is generated with Gmsh [23] on a sphere with center at  $\mathbf{x}_0 = \{0, 0, 0\}^T$  and radius  $R = 2000$  m and a cavity with radius  $r_0 = 20$  m, using 10-node quadratic tetrahedral finite elements. The frequency range of interest is defined by  $f_{\min} = f_{\max} = 5$  Hz. In order to avoid an excessive computational cost, the domain size is selected as  $R = 2\lambda_p^{\max}$ . According to equation (54), this choice provides a sufficiently low tolerance of  $1/(16\pi^2)$  on the total Newtonian noise. According to equations (56) and (58), however, the truncation errors on the bulk and surface contributions are expected to be larger. As the same finite element mesh is used for S- and P-wave propagation, the minimum finite element size  $l_e^{\min}$  is defined as  $\lambda_s^{\min}/n$  with the minimum shear wavelength  $\lambda_s^{\min} = C_s/f_{\max}$  and  $n = 4$ . The finite element mesh is graded with a distance-based power law (61) with linear grading ( $\alpha = 1$ ) departing from a minimum element size  $l_{e0} = \eta r_0/3$  with  $\eta = 0.3$ , so that  $l_{e0} = 0.1r_0$ , ensuring a smooth transition without over-refinement. This grading is applied until the element size  $l_e^{\min}$  imposed by the second criterion is reached.

Figure 3a compares the real part of the total Newtonian noise  $\delta\hat{a}_{tx}^{\text{num}}(\mathbf{x}_0, \omega)$  computed with the finite element approximation with the real part of the analytical solution  $\delta\hat{a}_{tx}^{\text{ref}}(\mathbf{x}_0, \omega)$  in the frequency range between 0.1 Hz and 10 Hz. The displacement  $\hat{\mathbf{u}}(\mathbf{x}_0, \omega)$  at the mirror in equation (48) is purely real, so that  $\delta\hat{a}_{tx}(\mathbf{x}_0, \omega)$  is also real. The imaginary part vanishes and therefore is not shown. The difference between the numerical and reference solution is expressed by the relative error:

$$\varepsilon_{tx}(\omega) = \frac{|\delta\hat{a}_{tx}^{\text{num}}(\mathbf{x}_0, \omega) - \delta\hat{a}_{tx}^{\text{ref}}(\mathbf{x}_0, \omega)|}{|\delta\hat{a}_{tx}^{\text{ref}}(\mathbf{x}_0, \omega)|}, \quad (62)$$

where  $|\cdot|$  denotes the magnitude of a complex number.

In the low frequency range considered, the total Newtonian noise  $\delta\hat{a}_{tx}^{\text{ref}}(\mathbf{x}_0, \omega)$  is nearly constant. The numerical prediction  $\delta\hat{a}_{tx}^{\text{num}}(\mathbf{x}_0, \omega)$  agrees very well with the analytical result at frequencies larger than 5 Hz, where the extension of the finite element mesh is sufficiently large, while the finite elements are still small enough to capture the wavelength. This is reflected by a low relative error  $\varepsilon_{tx}(\omega)$  in figure 3b. For lower frequencies, however, the numerical solution deviates from the reference solution due to the fixed domain size  $R = 2\lambda_p^{\text{max}}$ . The condition in equation (54) is no longer satisfied, and a larger domain size  $R$  would be required to maintain the same level of accuracy. The total Newtonian noise computed numerically from equation (31) is, as expected, equal to the sum of the bulk and surface contributions obtained from equations (37) and (45). The predicted bulk and surface contributions do not converge independently to their analytical values, since the tolerance criterion was applied only to the total Newtonian noise in equation (54), and not to the separate contributions.

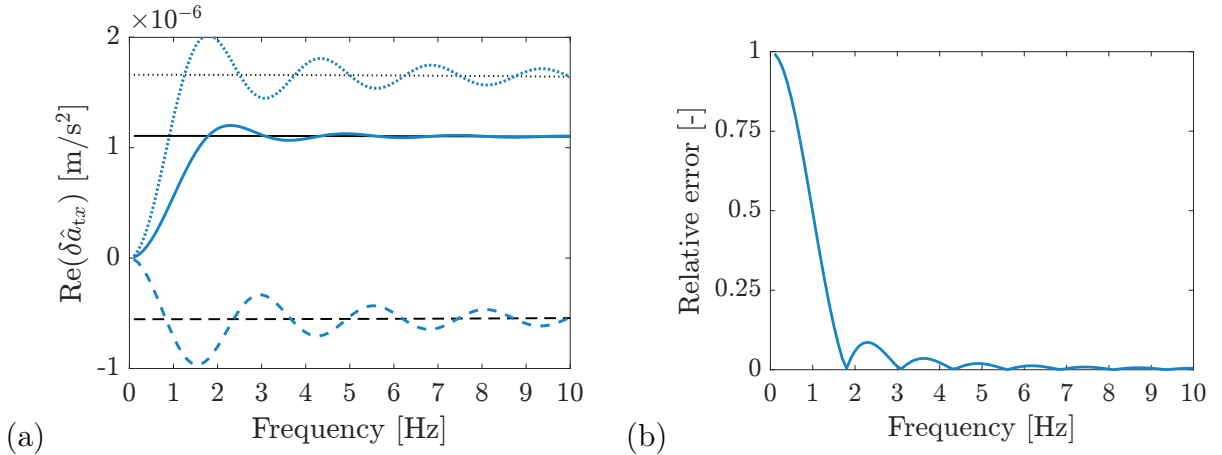


Figure 3: (a) Real part of the total Newtonian noise  $\delta\hat{a}_{tx}(\mathbf{x}_0, \omega)$  computed analytically (—) and with the numerical model (—), due to a plane harmonic P-wave in a linear elastic full space with a cavity with radius  $r_0 = 20$  m; the P-wave has unit amplitude and propagates in the direction  $\mathbf{e}_k = \{\frac{1}{\sqrt{2}}, \frac{1}{\sqrt{2}}, 0\}^T$ . The bulk contribution  $\delta\hat{a}_{bx}(\mathbf{x}_0, \omega)$  (..... and .....) and the surface contribution  $\delta\hat{a}_{sx}(\mathbf{x}_0, \omega)$  (--- and ---) are also shown. (b) Relative error  $\varepsilon_{tx}(\omega)$  on the total Newtonian noise.

#### 4.2. Plane harmonic S-wave in a full space

Newtonian noise is subsequently computed for a plane harmonic S-wave propagating in a homogeneous elastic full space with a wavelength  $\lambda_s$  that – in the low frequency range considered – is assumed to be much larger than the cavity radius  $r_0$ , so that wave scattering due to the cavity can again be ignored.

The displacement vector  $\hat{\mathbf{u}}(\mathbf{x}, \omega)$  due to a plane harmonic S-wave with unit amplitude propagating with velocity  $C_s$  in the direction  $\mathbf{e}_k$  and with polarization vector  $\mathbf{e}_s$  is equal to:

$$\hat{\mathbf{u}}(\mathbf{x}, \omega) = \exp(-ik_s \mathbf{e}_k \cdot \mathbf{x}) \mathbf{e}_s, \quad (63)$$

where  $k_s = \omega/C_s = 2\pi/\lambda_s$  is the shear wavenumber and  $\lambda_s$  is the corresponding wavelength. The polarization vector  $\mathbf{e}_s$  is orthogonal to the propagation direction  $\mathbf{e}_k$ .

Figure 3b shows the displacement component  $\hat{u}_z(\mathbf{x}, \omega)$  of a plane harmonic S-wave with unit amplitude and frequency of 5 Hz, propagating in the direction  $\mathbf{e}_k = \{1, 0, 0\}^T$  with polarization vector  $\mathbf{e}_s = \{0, 0, 1\}^T$  in a homogeneous linear elastic full space with properties as introduced before; the wave field is shown on a finite element mesh that will subsequently be used to compute the Newtonian noise. The wavelength  $\lambda_s = 500$  m at 5 Hz is much larger than the cavity radius  $r_0 = 20$  m, so that wave scattering by the cavity again can be disregarded.

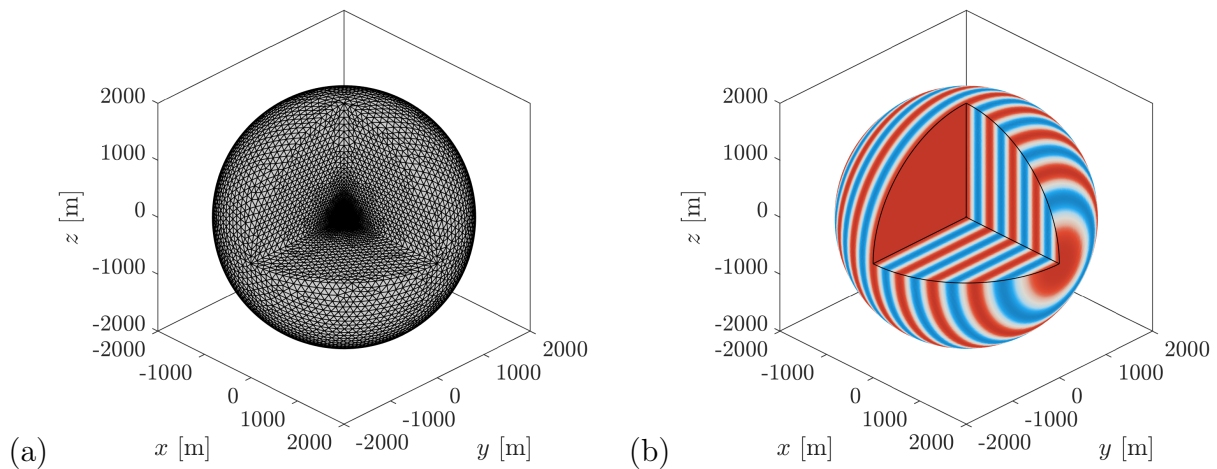


Figure 4: (a) Finite element mesh of a sphere with center at  $\mathbf{x}_0 = \{0, 0, 0\}^T$  and radius  $R = 2000$  m and a spherical cavity with radius  $r_0 = 20$  m, used to compute the Newtonian noise due to a plane harmonic S-wave in a frequency range around 5 Hz. (b) Displacement  $\hat{u}_z(\mathbf{x}, \omega)$  due to a plane harmonic S-wave with unit amplitude and frequency of 5 Hz propagating in the direction  $\mathbf{e}_k = \{1, 0, 0\}^T$  with polarization vector  $\mathbf{e}_s = \{0, 0, 1\}^T$ .

For a plane harmonic S-wave propagating in a homogeneous linear elastic full space, an analytical expression for the Newtonian noise can be derived if wave scattering by the cavity is ignored. Inserting equation (63) into equation (17) and evaluating the volume integral in spherical coordinates between radii  $r_0$  and  $R$  yields the following analytical expression for the Newtonian noise  $\delta \hat{\mathbf{a}}_t(\mathbf{x}_0, \omega)$  at the mirror position  $\mathbf{x}_0$  [4]:

$$\delta \hat{\mathbf{a}}_t(\mathbf{x}_0, \omega) = -4\pi\rho G \left( \frac{j_1(k_s r_0)}{k_s r_0} - \frac{j_1(k_s R)}{k_s R} \right) \hat{\mathbf{u}}(\mathbf{x}_0), \quad (64)$$

which, for a fullspace ( $R \rightarrow \infty$ ), gives:

$$\delta \hat{\mathbf{a}}_t(\mathbf{x}_0) = -4\pi\rho G \frac{j_1(k_s r_0)}{k_s r_0} \hat{\mathbf{u}}(\mathbf{x}_0). \quad (65)$$

Since the divergence of the displacement field associated with an S-wave is equal to zero, an S-wave causes no bulk contribution to the Newtonian noise and the total Newtonian noise is equal to the surface contribution.

The Newtonian noise is computed using the same finite element mesh as for the P-wave (figure 4a). Figure 5a compares the real part of the total Newtonian noise  $\delta\hat{a}_{tz}^{\text{num}}(\mathbf{x}_0, \omega)$  computed with the finite element approximation with the real part of the analytical solution  $\delta\hat{a}_{tz}^{\text{ref}}(\mathbf{x}_0, \omega)$  in the frequency range between 0.1 Hz and 10 Hz. The displacement  $\hat{\mathbf{u}}(\mathbf{x}_0, \omega)$  at the mirror in equation (65) is purely real, so that  $\delta\hat{a}_{tx}(\mathbf{x}_0, \omega)$  is also real. The imaginary part vanishes and therefore is not shown. In the low frequency range considered, the total Newtonian noise  $\delta\hat{a}_{tz}^{\text{ref}}(\mathbf{x}_0, \omega)$  is nearly constant. The numerical prediction  $\delta\hat{a}_{tz}^{\text{num}}(\mathbf{x}_0, \omega)$  agrees very well with the analytical result at frequencies larger than 5 Hz, where the extension of the finite element mesh is sufficiently large, while the finite elements are still small enough to capture the wavelength. This is reflected by a low relative error  $\varepsilon_{tz}(\omega)$  in figure 5b. It is noted that the numerical solution converges faster to the analytical reference solution for an S-wave than for a P-wave. This is expected, since the domain size  $R = 2\lambda_p^{\text{max}}$  was tailored to the wavelength of the P-wave. The wavelength of the S-wave is two times smaller, so that  $R = 4\lambda_s^{\text{max}}$ , which reduces the truncation error.

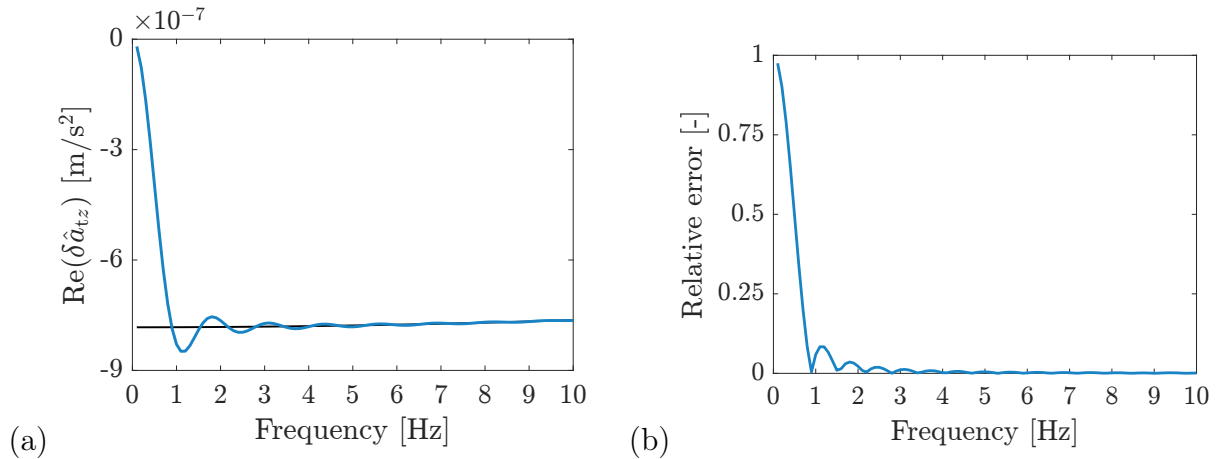


Figure 5: (a) Real part of the total Newtonian noise  $\delta\hat{a}_{tz}(\mathbf{x}_0)$  computed analytically (—) and with the numerical model (—), due to a plane harmonic S-wave in a linear elastic full space with a cavity with radius  $r_0 = 20$  m; the S-wave has unit amplitude and propagates in the direction  $\mathbf{e}_k = \{1, 0, 0\}^T$  with polarization vector  $\mathbf{e}_s = \{0, 0, 1\}^T$ . (b) Relative error  $\varepsilon_{tz}(\omega)$  on the total Newtonian noise.

### 4.3. Harmonic Rayleigh wave in an elastic halfspace

Next, the Newtonian noise on a test mass located at a position  $\mathbf{x}_0 = \{0, 0, -h\}^T$  above the free surface of a homogeneous linear elastic halfspace (figure 6) due to a harmonic Rayleigh wave with a wavelength  $\lambda_R$  is considered.

A Rayleigh wave propagates in a homogeneous linear elastic halfspace along the direction  $\mathbf{k}_k = k_R \mathbf{e}_k$ , with  $k_R = \omega/C_R$  the Rayleigh wavenumber,  $C_R$  the Rayleigh wave velocity, and  $\mathbf{e}_k = \{\cos \theta, \sin \theta, 0\}^T$  a unit vector in a plane perpendicular to the  $z$ -axis. The displacement vector  $\hat{\mathbf{u}}(\mathbf{x}, \omega)$  can be written as [24]:

$$\hat{\mathbf{u}}(\mathbf{x}, \omega) = (\hat{u}_k(z, \omega)\mathbf{e}_k + \hat{u}_z(z, \omega)\mathbf{e}_z) \exp(-i\mathbf{k}_k \cdot \mathbf{x}), \quad (66)$$

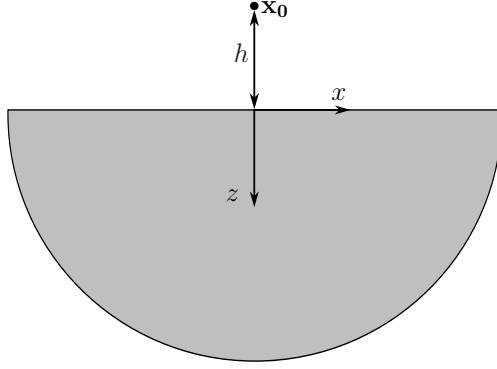


Figure 6: Homogeneous halfspace with a test mass at a position  $\mathbf{x}_0 = \{0, 0, -h\}^T$  above the free surface.

where the horizontal component  $\hat{u}_k(z, \omega)$  along  $\mathbf{e}_k$  is equal to:

$$\hat{u}_k(z, \omega) = +ik_{zs}A_s e^{-ik_{zs}z} - ik_R A_p e^{-ik_{zp}z}, \quad (67)$$

while the vertical component  $\hat{u}_z(z, \omega)$  is equal to:

$$\hat{u}_z(z, \omega) = -ik_R A_s e^{-ik_{zs}z} - ik_{zp} A_p e^{-ik_{zp}z}. \quad (68)$$

The vertical wavenumbers  $k_{zp}$  and  $k_{zs}$  follow from the dispersion relations:

$$k_{zp} = -i\sqrt{k_R^2 - k_p^2} \quad (69)$$

$$k_{zs} = -i\sqrt{k_R^2 - k_s^2} \quad (70)$$

where  $k_p = \omega/C_p$  and  $k_s = \omega/C_s$  are the dilatational and shear wave number. Negative imaginary vertical wavenumbers are selected since the real solution  $k_R$  of Rayleigh's cubic characteristic equation [24] is larger than both wavenumbers  $k_s$  and  $k_p$ . When these vertical wavenumbers are inserted in the displacement components (67) and (68), an evanescent or surface wave is obtained. The wave potentials  $A_p$  and  $A_s$  are components of the corresponding eigenvector (the Rayleigh wave mode) and related through the traction-free boundary condition at the free surface  $z = 0$ :

$$A_s = \beta A_p, \quad (71)$$

where the factor  $\beta$  is defined as:

$$\beta = \frac{2k_R k_{zp}}{k_s^2 - 2k_R^2}. \quad (72)$$

The Rayleigh wave mode is subsequently scaled so that the vertical displacement at the surface  $\hat{u}_z(0, \omega)$  is equal to 1:

$$\hat{u}_z(0, \omega) = -i(k_R \beta + k_{zp}) A_p = 1, \quad (73)$$

resulting in the following value for the potential  $A_p$ :

$$A_p = \frac{i}{k_R \beta + k_{zp}}. \quad (74)$$

Figure 7 shows the displacements  $\hat{u}_x(\mathbf{x}, \omega)$  and  $\hat{u}_z(\mathbf{x}, \omega)$  of a harmonic Rayleigh wave with unit amplitude and frequency of 5 Hz, propagating in the direction  $\mathbf{e}_k = \{1, 0, 0\}^T$  in a homogeneous linear elastic halfspace with the same properties as introduced for the full space. The wave field is shown on a finite element mesh that will subsequently be used to compute the Newtonian noise. Both components exhibit exponential decay with depth. The vertical displacement  $\hat{u}_z(\mathbf{x}, \omega)$  has unit amplitude at the surface, while the horizontal displacement  $\hat{u}_x(\mathbf{x}, \omega)$  changes sign around  $z \approx 0.2\lambda_R$ , which corresponds to the reversal of particle motion from retrograde near the surface to prograde at larger depth, characteristic of Rayleigh waves.

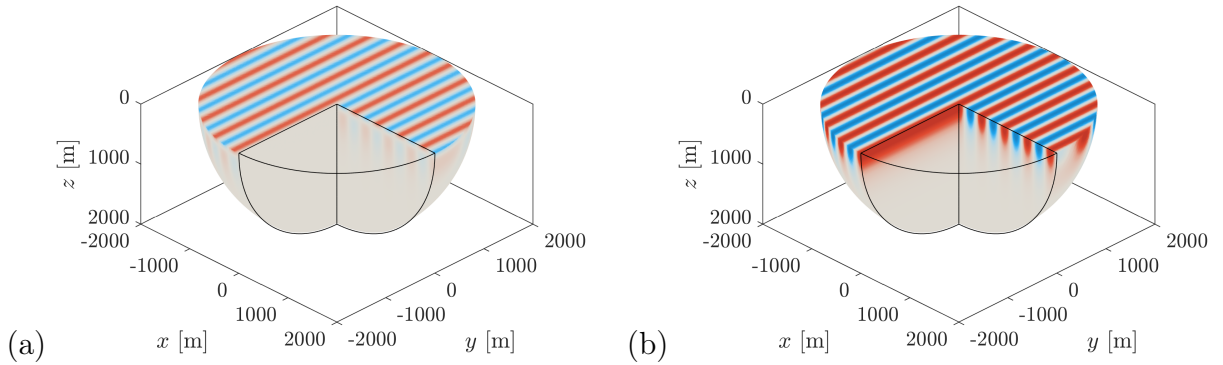


Figure 7: Displacement (a)  $\hat{u}_x(\mathbf{x}, \omega)$  and (b)  $\hat{u}_z(\mathbf{x}, \omega)$  due to a harmonic Rayleigh wave with unit amplitude and frequency of 5 Hz propagating in the direction  $\mathbf{e}_k = \{1, 0, 0\}^T$ .

The analytical expression of the total Newtonian noise for a harmonic Rayleigh wave propagating in a homogeneous linear elastic halfspace and a mirror located at  $\mathbf{x}_0 = \{0, 0, -h\}^T$  above the free surface is equal to [4]:

$$\delta \hat{\mathbf{a}}_t(\mathbf{x}_0, \omega) = 2\pi G \rho \gamma \exp(-k_R h) (\mathbf{i} \mathbf{e}_k - \mathbf{e}_z) \exp(-i \mathbf{k}_k \cdot \mathbf{x}_0), \quad (75)$$

where

$$\gamma = \frac{k_R (1 - \sqrt{k_{zp}/k_{zs}})}{i k_{zp} - k_R \sqrt{k_{zp}/k_{zs}}}. \quad (76)$$

The finite element formulation implemented in ANNA is subsequently used to compute the Newtonian noise due to a harmonic Rayleigh wave on a mirror located at  $\mathbf{x}_0 = \{0, 0, -20\}^T$ . A finite element mesh is created on a sphere with radius  $R = 2000$  m and center at  $\mathbf{x}_0$ , cut by the horizontal plane  $z = 0$  (figure 8a). The same meshing criteria and grading rule are applied as for the full space examples in the previous subsections. The minimum element size  $l_e^{\min}$  is defined by the minimum shear wavelength  $\lambda_s^{\min}/n$  with  $n = 4$ . The

finite element mesh is graded with a distance-based power law (61) where  $r = \|\mathbf{x} - \mathbf{x}_0\|$  is computed from the position  $\mathbf{x}_0$  of the test mass. Linear grading ( $\alpha = 1$ ) is applied departing from a minimum element size  $l_{e0} = \eta r_0/3$  with  $\eta = 0.3$ , until the element size  $l_e^{\min}$  is reached. This ensures a smooth transition with the smallest elements near the free surface closest to the mirror, as shown in figure 8.

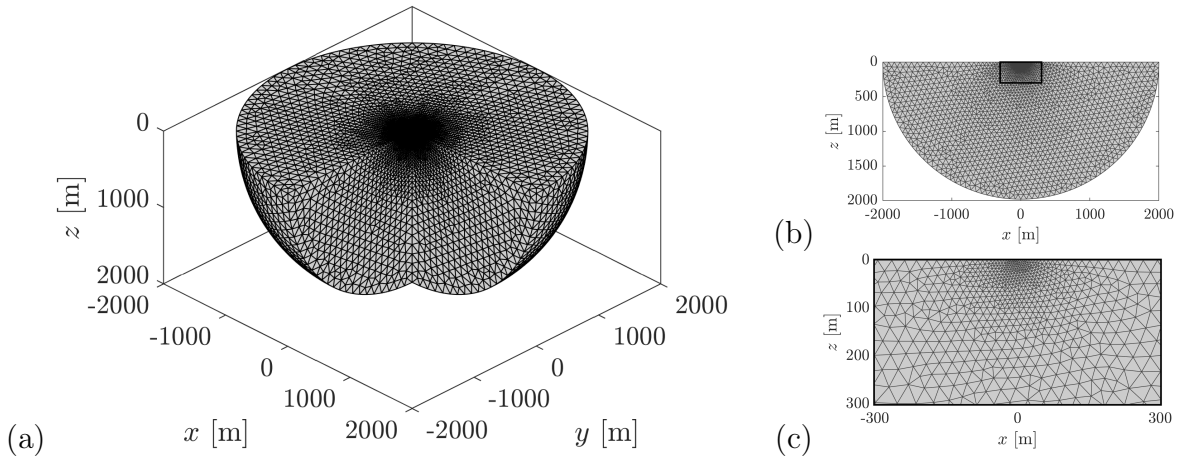


Figure 8: (a) Finite element mesh of a halfspace with radius  $R = 2000$  m and centre at  $\mathbf{x}_0 = \{0, 0, -20\}^T$  cut by the horizontal plane  $z = 0$ , used to compute the Newtonian noise due to a harmonic Rayleigh wave in a frequency range around 5 Hz. (b) Two-dimensional view along the plane  $x_2 = 0$  and (c) zoom near the free surface and mirror.

Figure 9a compares the imaginary part of the total Newtonian noise  $\delta\hat{a}_{tx}^{\text{num}}(\mathbf{x}_0, \omega)$  predicted with the finite element formulation and the analytical reference solution in the frequency range between 0.1 Hz and 10 Hz. Equation (75) shows that the horizontal component  $\delta\hat{a}_{tx}$  is purely imaginary. The real part vanishes and therefore is not shown. At low frequencies, the numerical result deviates from the reference solution due to the finite radius  $R$  of the domain, for similar reasons as discussed for the full space cases. At higher frequencies, excellent agreement is observed. This is reflected by the relative error  $\varepsilon_{tx}(\omega)$  in figure 9b, confirming that the adopted framework remains accurate for the halfspace configuration. The total Newtonian noise computed from equation (31) is, as expected, equal to the sum of the bulk and surface contributions obtained from equations (37) and (45).

Figure 10a compares the real part of the total Newtonian noise  $\delta\hat{a}_{tz}^{\text{num}}(\mathbf{x}_0, \omega)$  predicted with the finite element formulation and the analytical reference solution in the frequency range between 0.1 Hz and 10 Hz. According to equation (75), the vertical component  $\delta\hat{a}_{tz}$  is real. The imaginary part vanishes and therefore is not shown. As for the horizontal component, the low-frequency response is affected by the finite radius  $R$  of the domain, whereas excellent agreement is observed at higher frequencies, as reflected by the relative error  $\varepsilon_{tz}(\omega)$  in figure 10b.

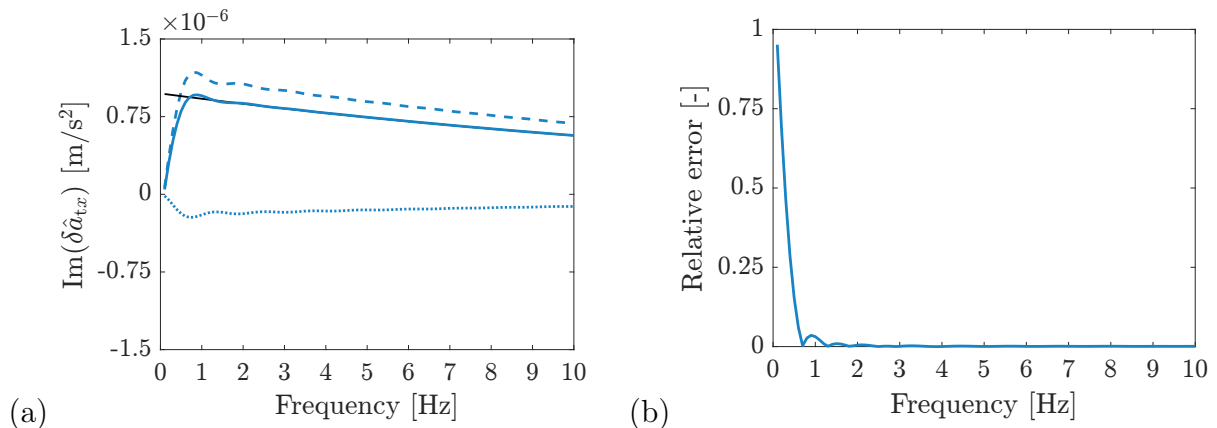


Figure 9: (a) Imaginary part of the total Newtonian noise  $\delta\hat{a}_{tx}(\mathbf{x}_0, \omega)$  computed analytically (—) and with the numerical model (—), due to a harmonic Rayleigh wave in a linear elastic halfspace with a test mass located at a height  $h = 20$  m above the free surface. The bulk contribution  $\delta\hat{a}_{bx}(\mathbf{x}_0, \omega)$  (.....) and the surface contribution  $\delta\hat{a}_{sx}(\mathbf{x}_0, \omega)$  (---) are also shown. (b) Relative error  $\varepsilon_{tx}(\omega)$  on the total Newtonian noise.

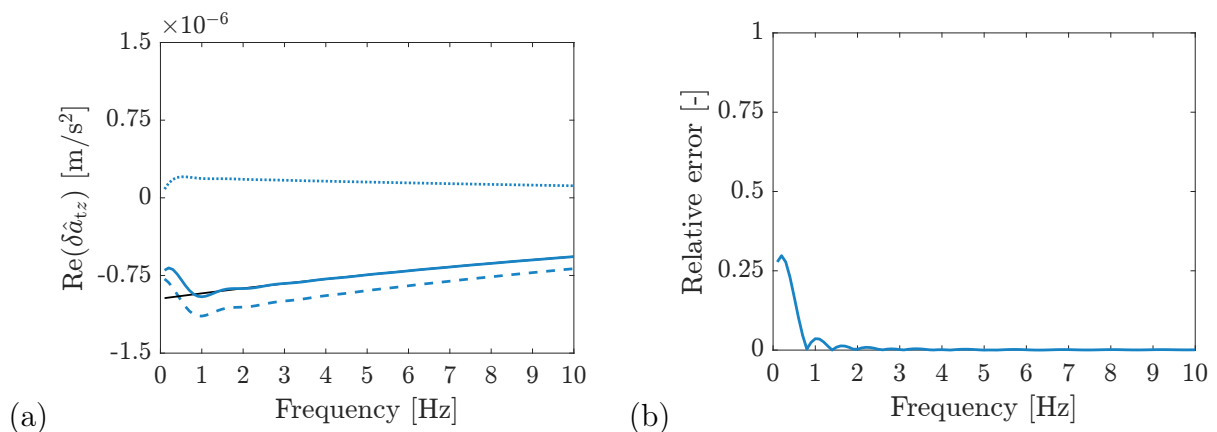


Figure 10: (a) Real part of the total Newtonian noise  $\delta\hat{a}_{tz}(\mathbf{x}_0, \omega)$  computed analytically (—) and with the numerical model (—), due to a harmonic Rayleigh wave in a linear elastic halfspace with a test mass located at a height  $h = 20$  m above the free surface. The bulk contribution  $\delta\hat{a}_{bz}(\mathbf{x}_0, \omega)$  (.....) and the surface contribution  $\delta\hat{a}_{sz}(\mathbf{x}_0, \omega)$  (---) are also shown. (b) Relative error  $\varepsilon_{tz}(\omega)$  on the total Newtonian noise.

## 5. Conclusions

This paper presents a toolbox ANNA Newtonian Noise Analysis that computes Newtonian noise on a mirror in a cavity from a 3D seismic wave field, using a finite element formulation. Gaussian quadrature on a 3D finite element mesh is used to numerically evaluate the volume and surface integrals that define the total Newtonian noise, as well as the bulk and surface contributions. ANNA is implemented in the MATLAB programming and numeric computing platform and is compatible with the open-source GNU Octave Scientific Programming Language; a Python [25] version is also available, making use of the high-performance NumPy package for array operations and numerical kernels for arrays [26].

Newtonian noise predicted with ANNA is verified for a suite of simplified problems for

which an analytical solution is available. Newtonian noise is predicted for a plane harmonic P- and S-wave propagating in a homogeneous linear elastic full space with a cavity with radius  $r_0$  and for a test mass at a distance  $h$  above the free surface of a homogeneous linear elastic halfspace where a harmonic Rayleigh wave propagates along the surface. When – in the frequency range of interest – proper criteria for finite element mesh extension and refinement are met carefully, the Newtonian noise predicted with ANNA is in very good agreement with the reference solutions. Therefore, ANNA can be employed with confidence to predict Newtonian noise from wave fields originating from different anthropogenic sources on soil domains with a more complex topography and stratification. The present verification can then be followed by a validation based on recorded seismic wave fields.

## Acknowledgements

Results presented in this paper have been obtained within the frame of the FWO-IRI projects I002123N "Essential Technologies for the Einstein Telescope" (2023-2024) and I000725N "ET-TECH: Empowering Tomorrow's Technological Horizons for Einstein Telescope" (2025) and the FWO Research Collaboration "Modelling external vibration sources" (2026). The financial support of the Research Foundation Flanders (FWO) is gratefully acknowledged.

## Data availability statement

The toolbox, a manual, and examples can be downloaded from <https://bwk.kuleuven.be/bwm/anna>.

## Appendix A. Reynolds' transport theorem

Assume a set of particles that occupy at time  $t = 0$  (in the reference configuration) a volume  $\Omega(\mathbf{X})$  with boundary  $\Gamma(\mathbf{X})$  and unit outward normal vector  $\mathbf{n}(\mathbf{X})$ . After deformation, at time  $t$  (in the actual configuration), these particles occupy a volume  $\Omega(\mathbf{x}, t)$  with boundary  $\Gamma(\mathbf{x}, t)$  and unit outward normal vector  $\mathbf{n}(\mathbf{x}, t)$  (figure A.1).

We consider a mass dependent scalar or vector quantity  $f(t)$ , defined in the actual configuration as the volume integral of a continuously differentiable scalar or vector quantity  $g(\mathbf{x}, t)$ :

$$f(t) = \int_{\Omega(\mathbf{x}, t)} g(\mathbf{x}, t) dv \quad (\text{A.1})$$

The scalar or vector quantity  $g(\mathbf{x}, t)$  can be defined, for example, as:

- the density  $\rho(\mathbf{x}, t)$ , in which case  $f(t)$  represents the mass of the particles contained in the volume  $\Omega(\mathbf{x}, t)$ ;
- the quantity  $\rho(\mathbf{x}, t)\mathbf{v}(\mathbf{x}, t)$ , such that the vector  $f(t)$  represents the linear momentum of the particles contained in the volume  $\Omega(\mathbf{x}, t)$ ;

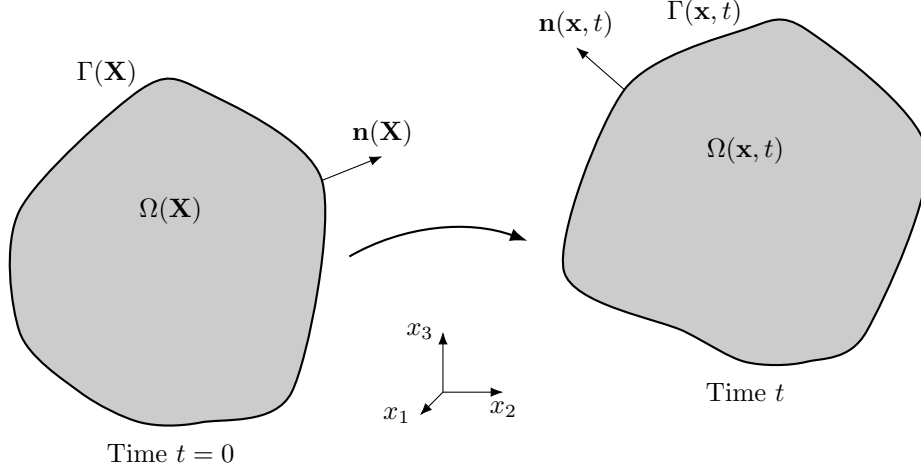


Figure A.1: Material volume  $\Omega(\mathbf{X})$  with boundary  $\Gamma(\mathbf{X})$  and unit outward normal vector  $\mathbf{n}(\mathbf{X})$  in the reference configuration at time  $t = 0$  and material volume  $\Omega(\mathbf{x}, t)$  with boundary  $\Gamma(\mathbf{x}, t)$  and unit outward normal vector  $\mathbf{n}(\mathbf{x}, t)$  in the actual configuration at time  $t$ .

- the quantity  $-G\rho(\mathbf{x}, t)/\|\mathbf{x} - \mathbf{x}_0\|$ , such that  $f(t)$  represents the gravitational potential of the test mass at position  $\mathbf{x}_0$ .

We need to evaluate the following total derivative with respect to time, as a rigorous representation of a "variation" of the quantity  $f(t)$  (in order to express conservation of mass, conservation of linear momentum, or a variation of the gravitational potential):

$$\frac{Df(t)}{Dt} = \frac{D}{Dt} \int_{\Omega(\mathbf{x}, t)} g(\mathbf{x}, t) dv \quad (\text{A.2})$$

Reynolds' transport theorem gives a formal expression of the total or material derivative with respect to time  $t$  of the quantity  $f(t)$ , or the variation of this quantity observed when following a set of particles that were contained in a volume  $\Omega(\mathbf{X})$  at time  $t = 0$  and are contained in a volume  $\Omega(\mathbf{x}, t)$  at time  $t$  [27]:

$$\frac{Df(t)}{Dt} = \int_{\Omega(\mathbf{x}, t)} \left[ \frac{Dg(\mathbf{x}, t)}{Dt} + g(\mathbf{x}, t) \nabla \cdot \mathbf{v}(\mathbf{x}, t) \right] dv \quad (\text{A.3})$$

$$= \int_{\Omega(\mathbf{x}, t)} \left[ \frac{\partial g(\mathbf{x}, t)}{\partial t} + \mathbf{v}(\mathbf{x}, t) \cdot \nabla g(\mathbf{x}, t) + g(\mathbf{x}, t) \nabla \cdot \mathbf{v}(\mathbf{x}, t) \right] dv \quad (\text{A.4})$$

$$= \int_{\Omega(\mathbf{x}, t)} \left[ \frac{\partial g(\mathbf{x}, t)}{\partial t} + \nabla \cdot (g(\mathbf{x}, t) \mathbf{v}(\mathbf{x}, t)) \right] dv \quad (\text{A.5})$$

$$= \int_{\Omega(\mathbf{x}, t)} \frac{\partial g(\mathbf{x}, t)}{\partial t} dv + \int_{\Gamma(\mathbf{x}, t)} g(\mathbf{x}, t) \mathbf{v}(\mathbf{x}, t) \cdot \mathbf{n}(\mathbf{x}, t) da \quad (\text{A.6})$$

The first term on the right-hand side of equation (A.6) is the instantaneous variation of the quantity  $g(\mathbf{x}, t)$  or the rate of change of  $g(\mathbf{x}, t)$  at time  $t$  for all particles contained in

the volume  $\Omega(\mathbf{x}, t)$ . The second term is the flux of the property  $g(\mathbf{x}, t)$  as particles exit the volume  $\Omega(\mathbf{x}, t)$  through its surface  $\Gamma(\mathbf{x}, t)$  with a normal velocity  $\mathbf{v}(\mathbf{x}, t) \cdot \mathbf{n}(\mathbf{x}, t)$ , where  $\mathbf{n}(\mathbf{x}, t)$  is the unit outward normal vector to the boundary  $\Gamma(\mathbf{x}, t)$ . This term originates from the fact that the volume  $\Omega(\mathbf{x}, t)$  with boundary  $\Gamma(\mathbf{x}, t)$  that contains a fixed amount of material has moved during a time step  $\Delta t$  to a volume  $\Omega(\mathbf{x}, t + \Delta t)$  with boundary  $\Gamma(\mathbf{x}, t + \Delta t)$  (figure A.2).

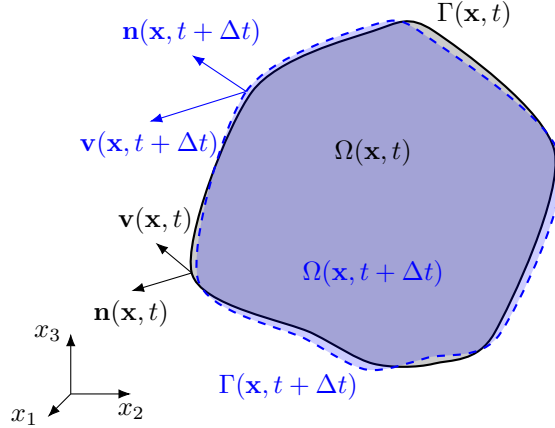


Figure A.2: Material volume  $\Omega(\mathbf{x}, t)$  with boundary  $\Gamma(\mathbf{x}, t)$  in the actual configuration at time  $t$  and material volume  $\Omega(\mathbf{x}, t + \Delta t)$  with boundary  $\Gamma(\mathbf{x}, t + \Delta t)$  in the actual configuration at time  $t + \Delta t$ .

In the particular case where the volume  $\bar{\Omega}$  is a fixed region in space (or a control volume) with boundary  $\bar{\Gamma}$ , the integration over the volume is decoupled from partial integration and Reynolds' transport theorem can be expressed as [27]:

$$\frac{Df(t)}{Dt} = \frac{\partial}{\partial t} \int_{\bar{\Omega}} g(\mathbf{x}, t) dv + \int_{\bar{\Gamma}} g(\mathbf{x}, t) \mathbf{v}(\mathbf{x}, t) \cdot \mathbf{n}(\mathbf{x}, t) da \quad (\text{A.7})$$

The first term on the right-hand side of equation (A.7) is the rate of change of the integral of the quantity  $g(\mathbf{x}, t)$  over the volume  $\bar{\Omega}$  due to its explicit dependence on time. The second term is the flux of the property  $g(\mathbf{x}, t)$  as particles exit the volume  $\bar{\Omega}$  through its fixed boundary  $\bar{\Gamma}$  with a normal velocity  $\mathbf{v}(\mathbf{x}, t) \cdot \mathbf{n}(\mathbf{x}, t)$ .

## Appendix B. Conservation of mass

The total mass  $M(t)$  of all particles contained at time  $t$  in a volume  $\Omega(\mathbf{x}, t)$  is equal to:

$$M(t) = \int_{\Omega(\mathbf{x}, t)} \rho(\mathbf{x}, t) dv \quad (\text{B.1})$$

where  $\rho(\mathbf{x}, t)$  is the density of the material.

Conservation of mass is expressed as:

$$\frac{DM(t)}{Dt} = \frac{D}{Dt} \int_{\Omega(\mathbf{x}, t)} \rho(\mathbf{x}, t) dv = 0 \quad (\text{B.2})$$

and elaborated in one of the following forms applying Reynolds' transport theorem:

$$\int_{\Omega(\mathbf{x},t)} \left[ \frac{D\rho(\mathbf{x},t)}{Dt} + \rho(\mathbf{x},t)\nabla \cdot \mathbf{v}(\mathbf{x},t) \right] dv = 0 \quad (\text{B.3})$$

$$\Leftrightarrow \int_{\Omega(\mathbf{x},t)} \left[ \frac{\partial\rho(\mathbf{x},t)}{\partial t} + \mathbf{v}(\mathbf{x},t) \cdot \nabla\rho(\mathbf{x},t) + \rho(\mathbf{x},t)\nabla \cdot \mathbf{v}(\mathbf{x},t) \right] dv = 0 \quad (\text{B.4})$$

$$\Leftrightarrow \int_{\Omega(\mathbf{x},t)} \left[ \frac{\partial\rho(\mathbf{x},t)}{\partial t} + \nabla \cdot (\rho(\mathbf{x},t)\mathbf{v}(\mathbf{x},t)) \right] dv = 0 \quad (\text{B.5})$$

$$\Leftrightarrow \int_{\Omega(\mathbf{x},t)} \frac{\partial\rho(\mathbf{x},t)}{\partial t} dv + \int_{\Gamma(\mathbf{x},t)} \rho(\mathbf{x},t)\mathbf{v}(\mathbf{x},t) \cdot \mathbf{n}(\mathbf{x},t) da = 0 \quad (\text{B.6})$$

In the special case where the volume  $\bar{\Omega}$  is a fixed region in space (or a control volume) with boundary  $\bar{\Gamma}$ , the integration over the volume is decoupled from partial integration [27], and conservation of mass reads as:

$$\frac{\partial}{\partial t} \int_{\bar{\Omega}} \rho(\mathbf{x},t) dv + \int_{\bar{\Gamma}} \rho(\mathbf{x},t)\mathbf{v}(\mathbf{x},t) \cdot \mathbf{n}(\mathbf{x},t) da = 0 \quad (\text{B.7})$$

Equation (B.7) expresses that the variation of mass in the volume  $\bar{\Omega}$  as a function of time (the first term) is equal to minus the flux of mass through the boundary  $\bar{\Gamma}$  (the second term) with a normal velocity  $\mathbf{v}(\mathbf{x},t) \cdot \mathbf{n}(\mathbf{x},t)$ .

As conservation of mass must hold for any volume  $\Omega(\mathbf{x},t)$ , the integrand in equations (B.3-B.5) must also be equal to zero:

$$\frac{D\rho(\mathbf{x},t)}{Dt} + \rho(\mathbf{x},t)\nabla \cdot \mathbf{v}(\mathbf{x},t) = 0 \quad (\text{B.8})$$

$$\Leftrightarrow \frac{\partial\rho(\mathbf{x},t)}{\partial t} + \mathbf{v}(\mathbf{x},t) \cdot \nabla\rho(\mathbf{x},t) + \rho(\mathbf{x},t)\nabla \cdot \mathbf{v}(\mathbf{x},t) = 0 \quad (\text{B.9})$$

$$\Leftrightarrow \frac{\partial\rho(\mathbf{x},t)}{\partial t} + \nabla \cdot (\rho(\mathbf{x},t)\mathbf{v}(\mathbf{x},t)) = 0 \quad (\text{B.10})$$

In a rate-independent form where the total derivative of the mass potential with respect to time is replaced by a variation, and the velocity vector is replaced by the displacement vector, the variation of the density becomes:

$$\delta\rho(\mathbf{x},t) + \nabla \cdot (\rho(\mathbf{x},t)\mathbf{u}(\mathbf{x},t)) = 0 \quad (\text{B.11})$$

## References

- [1] ET Steering Committee Editorial Team. *Design Report Update 2020 for the Einstein Telescope*. September 2020.
- [2] F. Amann et al. Site-selection criteria for the Einstein Telescope. *Review of Scientific Instruments*, 91:094504, 2020.

- [3] J.C. Driggers, J. Harms, and R.X. Adhikari. Subtraction of Newtonian noise using optimized sensor arrays. *Physical Review D*, 86:102001, 2012.
- [4] J. Harms. Terrestrial gravity fluctuations. *Living Reviews in Relativity*, 22:6, 2019.
- [5] E. Kausel and J.M. Roësset. Stiffness matrices for layered soils. *Bulletin of the Seismological Society of America*, 71(6):1743–1761, 1981.
- [6] M. Schevenels, S. François, and G. Degrande. EDT: An ElastoDynamics Toolbox for MATLAB. *Computers & Geosciences*, 35(8):1752–1754, 2009. <http://dx.doi.org/10.1016/j.cageo.2008.10.012>.
- [7] G. Lombaert, G. Degrande, J. Kogut, and S. François. The experimental validation of a numerical model for the prediction of railway induced vibrations. *Journal of Sound and Vibration*, 297(3-5):512–535, 2006.
- [8] G. Lombaert and G. Degrande. Ground-borne vibration due to static and dynamic axle loads of InterCity and high speed trains. *Journal of Sound and Vibration*, 319(3-5):1036–1066, 2009.
- [9] G. Lombaert, S. François, and G. Degrande. TRAFFIC Matlab toolbox for traffic induced vibrations. Report BWM-2012-10, Department of Civil Engineering, KU Leuven, November 2012. User’s Guide Traffic 5.2.
- [10] X. Sheng, C.J.C. Jones, and D.J. Thompson. A theoretical model for ground vibration from trains generated by vertical track irregularities. *Journal of Sound and Vibration*, 272(3):937–965, 2004.
- [11] E. Ntotsios, D.J. Thompson, and M.F.M. Hussein. The effect of track load correlation on ground-borne vibration from railways. *Journal of Sound and Vibration*, 402:142–163, 2017.
- [12] E. Ntotsios, D.J. Thompson, and M.F.M. Hussein. A comparison of ground vibration due to ballasted and slab tracks. *Transportation Geotechnics*, 21(100256), 2019.
- [13] P. Jean. A 3D FEM/BEM code for ground-structure interaction: implementation strategy including the multi-traction problem. *Engineering Analysis with Boundary Elements*, 59:52–61, 2015.
- [14] Y.B. Yang and H.H. Hung. Soil vibrations caused by underground moving trains. *Journal of Geotechnical and Geoenvironmental Engineering, Proceedings of the ASCE*, 134(11):1633–1644, 2008.
- [15] Y.B. Yang and H.H. Hung. *Wave propagation for train-induced vibrations*. World Scientific, Taipei, 2009.

- [16] S. François, M. Schevenels, G. Lombaert, and G. Degrande. A 2.5D displacement based PML for elastodynamic wave propagation. *International Journal for Numerical Methods in Engineering*, 90(7):819–837, 2012.
- [17] L. Andersen. Influence of dynamic soil-structure interaction on building response due to ground vibration. In *Proceedings of the 8th European Conference on Numerical Methods in Geotechnical Engineering*, Delft, The Netherlands, June 2014.
- [18] S. François, M. Schevenels, G. Lombaert, P. Galvín, and G. Degrande. A 2.5D coupled FE-BE methodology for the dynamic interaction between longitudinally invariant structures and a layered halfspace. *Computer Methods in Applied Mechanics and Engineering*, 199(23-24):1536–1548, 2010.
- [19] M. Papadopoulos, S. François, G. Degrande, and G. Lombaert. The influence of uncertain local subsoil conditions on the response of buildings to ground vibration. *Journal of Sound and Vibration*, 418:200–220, 2018.
- [20] I. Mazzieri, M. Stupazzini, R. Guidotti, and C. Smerzini. SPEED: SPectral Elements in Elastodynamics with Discontinuous Galerkin: a non-conforming approach for 3D multi-scale problems. *International Journal for Numerical Methods in Engineering*, 95(12):991–1010, 2013.
- [21] S. François, M. Schevenels, D. Dooms, M. Jansen, J. Wambacq, G. Lombaert, G. Degrande, and G. De Roeck. Stabil: an educational Matlab toolbox for static and dynamic structural analysis. *Computer Applications in Engineering Education*, 29(5):1–18, 2021.
- [22] A. Quarteroni, F. Saleri, and P. Gervasio. *Scientific computing with MATLAB and Octave*, volume 2. Springer, 2006.
- [23] C. Geuzaine and J.-F. Remacle. Gmsh: a three-dimensional finite element mesh generator with built-in pre- and post-processing facilities. *International Journal for Numerical Methods in Engineering*, 79(11):1309–1331, 2009.
- [24] J.W.S. Rayleigh. On waves propagated along the plane surface of an elastic solid. *Proceedings of the London Mathematical Society*, 17:4–11, 1887.
- [25] Travis E Oliphant. Python for scientific computing. *Computing in science & engineering*, 9(3):10–20, 2007.
- [26] Charles R Harris, K Jarrod Millman, Stéfan J Van Der Walt, Ralf Gommers, Pauli Virtanen, David Cournapeau, Eric Wieser, Julian Taylor, Sebastian Berg, Nathaniel J Smith, et al. Array programming with numpy. *Nature*, 585(7825):357–362, 2020.
- [27] P. Papadopoulos. *ME185 Introduction to Continuum Mechanics*. Department of Mechanical Engineering, University of California, Berkeley, USA, September 2020.